Topology- and Gradient-Guided Knowledge Distillation for Point Cloud Semantic Segmentation

Anonymous authors
Paper under double-blind review

Abstract

Point cloud processing has gained significant attention due to its critical role in applications such as autonomous driving and 3D object recognition. However, deploying high-performance models like Point Transformer V3 in resource-constrained environments remains challenging due to their high computational and memory demands. This work introduces a novel distillation framework that leverages topology-aware representations and gradient-guided knowledge distillation to effectively transfer knowledge from a high-capacity teacher to a lightweight student model. Our approach captures the underlying geometric structures of point clouds while selectively guiding the student model's learning process through gradient-based feature alignment. Experimental results in the Nuscenes, SemanticKITTI, and Waymo datasets demonstrate that the proposed method achieves competitive performance, with an approximately 16× reduction in model size and up to 1.9× decrease in inference time compared to its teacher model. Notably, on NuScenes, our method achieves competitive performance among knowledge distillation techniques trained solely on LiDAR data, surpassing prior knowledge distillation baselines in segmentation performance. Our implementation is available anonymously at `https://anonymous.4open.science/r/PTv3-distill-4E9E`.

1 Introduction

Point cloud data are a critical representation of 3D geometry and have become essential in a wide range of applications, from autonomous driving and robotic navigation to urban mapping Zhou & Tuzel (2018); Geiger et al. (2012); Gomez-Ojeda et al. (2016); Oh & Watanabe (2002). Recent advances in deep learning have enabled significant progress in point cloud processing, with models such as Point Transformer V3 Wu et al. (2024) setting new benchmarks in accuracy and robustness. Despite the success of models like Point Transformer V3, their high computational demands and memory requirements Golla & Klein (2015); Cao et al. (2019) pose challenges for deployment in resource-constrained environments, such as edge devices or real-time systems. To address this issue, various model compression strategies have been introduced, including methods such as network pruning Han et al. (2016); Liu et al. (2019b); Louizos et al. (2018), quantization Choi et al. (2019); Dong et al. (2022); Nagel et al. (2019), lightweight model architectures Howard et al. (2019); Ma et al. (2018), and knowledge distillation Zhang et al. (2023); Hou et al. (2022a); Zhang et al. (2024).

Knowledge distillation is a machine learning technique that aims to transfer knowledge from a large and high capacity model to a smaller and more efficient model Hinton et al. (2014); Romero et al. (2015); Sanh et al. (2019). This approach allows the student model to approximate the performance of the teacher while being computationally less demanding, making it suitable for deployment in resource-constrained environments such as edge devices or mobile platforms. Over the years, knowledge distillation has been effectively applied in various domains, including image recognition Romero et al. (2015); Liu et al. (2019a) and natural language processing Hahn & Choi (2019); He et al. (2021); Rashid et al. (2021), demonstrating its versatility and impact. Recently, several approaches have been introduced to incorporate knowledge distillation into 3D detection tasks using point cloud data Guo et al. (2021b); Zhang et al. (2024). However, these methods

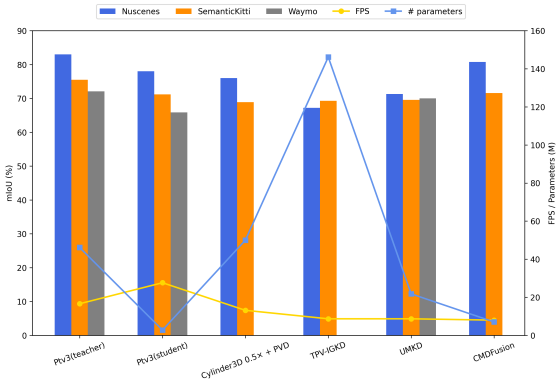

(a) Performance comparison

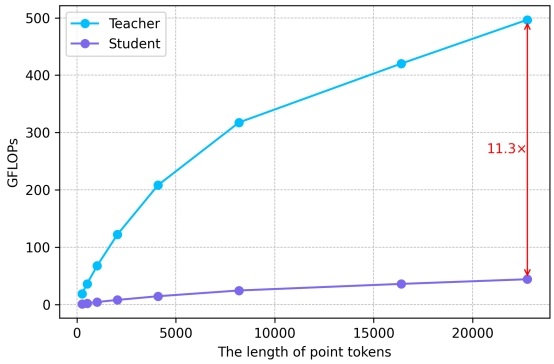

(b) GFLOPs comparison

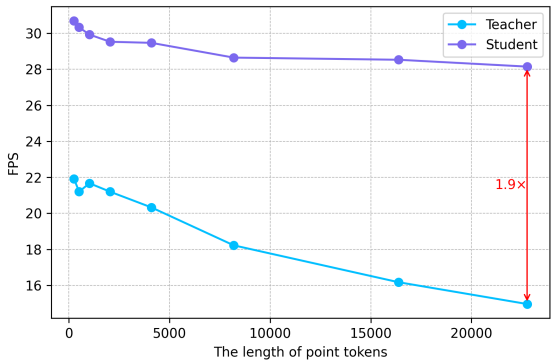

(c) FPS comparison

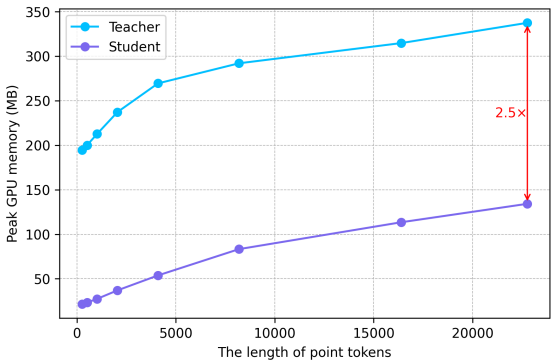

(d) Peak Memory Comparison

Figure 1: Comprehensive comparisons between our proposed method and state-of-the-art knowledge distillation baselines across multiple evaluation metrics Hou et al. (2022c); Li et al. (2024b); Sun et al. (2024); Cen et al. (2024). (a) The radar chart demonstrates that our method achieves consistently better mIoU on three key datasets (NuScenes, SemanticKITTI, and Waymo), along with favorable FPS and memory efficiency. (b)-(d) As the input point token length increases, our approach maintains lower GPU memory usage and FLOPs, while sustaining significantly faster inference speed. (d) Peak GPU memory usage during inference, measured using max memory allocated function in Torch. This metric reflects the highest amount of memory used by the PyTorch tensors by the caching allocator during the inference phase. Notably, this value may differ significantly from the memory reported by the PyTorch Profiler, as it includes temporary allocations used by CUDA kernels.

focus primarily on multimodal student-teacher selection in a multimodal context, often overlooking the unique geometric characteristics of point clouds.

To overcome these deployment hurdles, we propose a framework combining topology-aware representations with gradient-guided distillation. The framework leverages the inherent geometric and structural properties of point clouds to preserve critical topological information during the distillation process. By integrating gradient-based guidance, the proposed approach selectively emphasizes salient geometric features that contribute most significantly to the model's performance, enabling efficient knowledge transfer from a high-capacity teacher model to a lightweight student model. This strategy ensures that the student model retains competitive accuracy while significantly reducing computational and memory requirements, making it suitable for real-time and edge-based applications.

Extensive experiments on the proposed method have been conducted to demonstrate the effectiveness of our approach over previous knowledge distillation methods. Our main contributions can be summarized as follows.

- We propose a novel distillation framework that integrates topology-aware knowledge representation and gradient-guided distillation techniques, addressing the challenges of deploying high-performance point cloud models in resource-constrained environments.

- The framework leverages the unique geometric and structural properties of point clouds, embedding topological information into the distillation process to ensure the preservation of critical features necessary for accurate predictions.

- By incorporating gradient-guided distillation, our method selectively emphasizes salient features, enabling efficient and effective knowledge transfer from the teacher model to the student model.

- Extensive experimental results on popular benchmark datasets, such as Nuscenes reveal that our approach achieves up to a 16× reduction in the number of parameters and a 77.75% reduction in CUDA memory consumption in linear operations and a 2.5× lower in peak CUDA memory usage during inference while maintaining accuracy within 5% of state-of-the-art of non-distilled methods.

2 Related Works

3D Point Cloud Processing. The representation of 3D data using point clouds has become increasingly prominent in domains such as autonomous driving, robotics, and 3D reconstruction. Traditional deep learning approaches for understanding 3D point clouds can be categorized into three main types: projection-based, voxel-based, and point-based methods Halperin & Eisl (2025). Projection-based techniques map 3D points onto 2D image planes and employ 2D CNN backbones for feature extractionChen et al. (2017); Lang et al. (2019); Li et al. (2016), often losing geometric details in the process. Voxel-based methods convert point clouds into structured voxel grids, allowing 3D convolutions with sparse convolution enhancing efficiencyChoy et al. (2019); Song et al. (2017); Wang et al. (2017), though they encounter scalability issues due to limited grid resolution, sparse and irregular data distribution, and kernel size constraints. In contrast, point-based methods directly process raw point cloudsMa et al. (2022); Qi et al. (2017); Thomas et al. (2019); Zhao et al. (2019), with early approaches struggling to capture local structures until recent transformer-based architectures improved performance by modeling long-range dependencies and adapting to irregular distributionsGuo et al. (2021a); Robert et al. (2023); Wu et al. (2022b); Yang et al. (2023). Furthermore, hybrid methods that integrate point-voxel or graph-based representations have emerged to balance accuracy and efficiency. Across these approaches, challenges such as noise, occlusion, and varying point density in real-world data continue to impact performance.

Point Transformer Architecture. Transformer architectures improve point-based methods by leveraging self-attention to capture local and global dependencies effectively, outperforming CNN-based and voxel-based approaches. Early models like PCT Guo et al. (2021a) and Point Transformer Wu et al. (2022b) demonstrated strong performance in classification and segmentation tasks. Point Transformer V1 (PTv1) Zhao et al. (2021) extended the transformers to unordered 3D point sets by vector self-attention and local attention based on kNN, improving spatial modeling, but suffering from high memory and computational costs. Point Transformer V2 (PTv2) Wu et al. (2022a) introduced group vector attention and grid-based grouping to enhance scalability and reduce parameters, although kNN remained a bottleneck limiting long-range dependency capture. Point Transformer V3 (PTv3) Wu et al. (2024) shifted toward simplicity by serializing point clouds using space-filling curves and employing serialized patch attention, greatly expanding receptive fields, and eliminating kNN dependence. PTv3 achieved a 3.3× speedup and a 10.2× memory reduction over PTv2, establishing state-of-the-art results in diverse 3D tasks. However, PTv3's preprocessing overhead, increased latency on dense clouds, and dependence on high-end hardware limit its applicability in real-time, resource-constrained scenarios.

Knowledge distillation (KD) is a model-independent technique that improves student model training by transferring knowledge from a pre-trained teacher model, offering a way to enhance the efficiency of models such as Point Transformer V3 (PTv3). Early KD methods Hinton et al. (2015) matched softmax outputs for classification, while later studies Liu et al. (2019a); Romero et al. (2015); Tung & Mori (2019) extended KD to intermediate layers, capturing richer geometric and contextual information crucial for point-cloud data.

KD is particularly promising for addressing the challenges of PTv3 in real-time deployment by enabling lighter, faster models.

Topological Distillation leverages topological data analysis (TDA) to transfer global structural features. Methods like TGD Jeon et al. (2024) and TopKD Kim et al. (2024) distill topological knowledge through persistence images (PI) and diagrams (PD), improving the alignment of student-teacher. Despite benefits, topological distillation faces scalability challenges due to the computational cost of TDA and potential errors from PD-to-PI approximations. Its effectiveness across diverse point cloud tasks and noisy data remains limited, requiring further research for efficient usage.

Differentiable Topological Layers. Integrating persistent homology into deep learning requires overcoming the non-differentiability of the discrete persistence map. Early approaches relied on post-hoc topological descriptors like Persistence Imagesor Landscapes, which are vectorizable but decouple the topology from the optimization loop. More recent methods aim for end-to-end differentiability. Topological Autoencoders Moor et al. (2020) introduced a topological signature loss that aligns the persistence diagrams of the data and latent space, utilizing the fact that persistence values are locally continuous with respect to input distances. PersLay Carrière et al. (2020) and Differentiable Topology Layers Brüel-Gabrielsson et al. (2020) formalized this by treating persistence diagrams as differentiable layers, learning optimal vectorizations. However, these methods often rely on soft approximations or kernel-based smoothing to handle gradients. In contrast, our approach leverages the *inverse map theorem* to route gradients directly through the exact critical edges of the Vietoris-Rips complex Poulenard et al. (2018), enabling precise structure alignment without approximation artifacts.

3 Methodology

3.1 Overview of the Framework

Our framework introduces a topology-guided distillation approach designed to transfer both structural complexity and semantic precision from a high-capacity teacher to a lightweight student. As illustrated in Figure 2, the student mimics the teacher through a multi-objective optimization strategy. Beyond standard output replication, we introduce a Topological Distillation mechanism that aligns the underlying geometric manifolds of the feature spaces.

The student model optimizes the following objectives:

- **Targeted Topological Distillation**: We employ a differentiable Vietoris-Rips filtration to extract exact persistence diagrams (H_0 and H_1) from both models. A persistence-weighted Chamfer loss forces the student to replicate significant topological features (clusters and loops) while ignoring noise.
- **Gradient-Guided Feature Alignment**: We utilize task-specific gradients to identify and align spatially salient feature regions, ensuring the student focuses on semantically critical points.
- **Distribution Matching**: We employ Kullback-Leibler Divergence (KLD) on the soft logits to transfer the teacher's class-wise confidence distributions.

3.2 Manifold Alignment via Differentiable Topology

Standard losses like MSE focus on point-to-point accuracy but ignore the global shape of the data. This often causes lightweight models to learn fractured manifolds—getting the points roughly correct, but breaking the underlying geometric structure.

3.2.1 Differentiable Vietoris-Rips Filtration

The core challenge in integrating Topological Data Analysis (TDA) into deep learning is the discrete nature of the persistence map. Standard algorithms for computing persistent homology rely on combinatorial

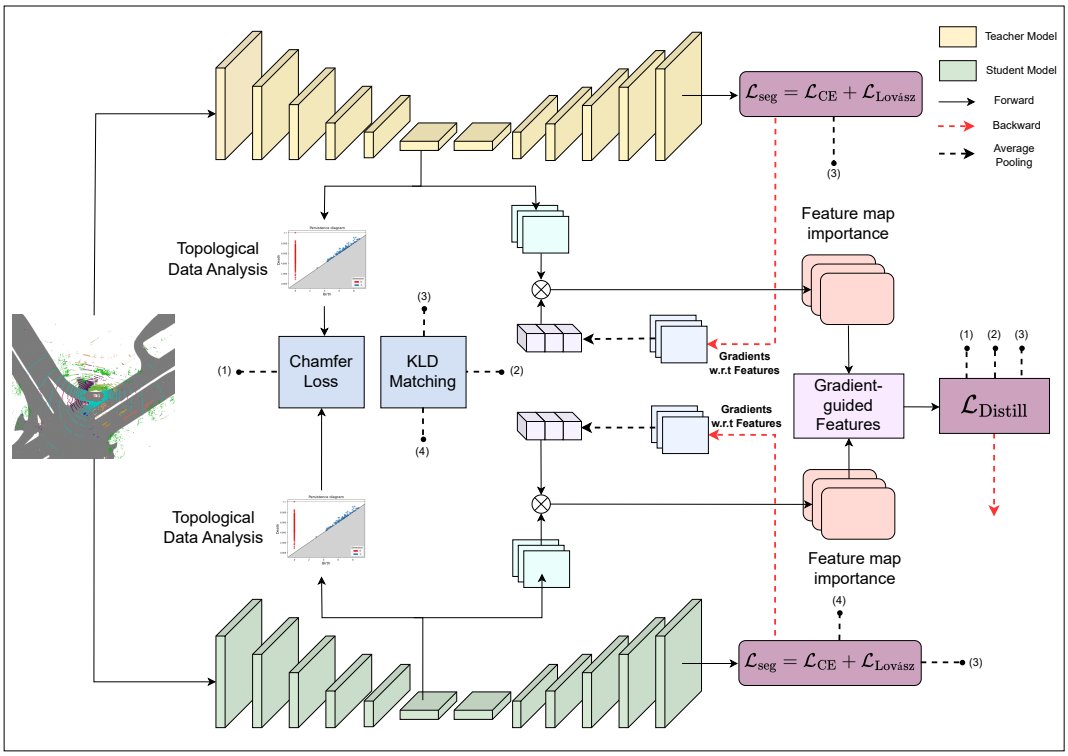

Figure 2: Overview of the proposed framework. The distillation process is driven by (1) **Topological Data Analysis (TDA)**, which aligns the persistence diagrams of feature manifolds using a weighted Chamfer distance; (2) **Logits Distillation** via KLD; and (3) **Gradient-Guided Feature Alignment**. The combination enables the lightweight student to capture global geometry (H_1 loops, H_0 clusters) and local semantics simultaneously.

operations (matrix reduction over finite fields) which are non-differentiable. To overcome this, we exploit the fact that for Vietoris–Rips filtrations the birth/death times are piecewise-smooth functions of the pairwise distances: each birth/death value equals the filtration value of a paired creator/destroyer simplex, whose filtration value is the maximum edge length within that simplex. In practice, we run Ripser in persistent cohomology mode (cocycles) and record, for each finite persistence pair, the paired creator simplex $\sigma_b(k)$ and destroyer simplex $\sigma_d(k)$. During backpropagation we route diagram gradients to the maximizing edge(s) of $\sigma_b(k)$ and $\sigma_d(k)$ (uniformly at ties), yielding a valid Clarke subgradient almost everywhere.

Problem. Let $f_\theta : \mathcal{X} \to \mathcal{H}$ be the encoder parameterized by θ. For an input X, we obtain feature embeddings $H = f_\theta(X) = \{h_1, \ldots, h_N\} \subset \mathbb{R}^C$. The persistence map $\Psi : H \to \mathcal{D}$ involves sorting edge lengths and reducing a boundary matrix over a finite field $\mathbb{Z}_2$, operations which usually have zero gradients almost everywhere.

Solution. Although persistent homology is computed by discrete operations (sorting simplices and reducing a boundary matrix over $\mathbb{Z}_2$), the resulting diagram coordinates are piecewise-smooth functions of the underlying edge lengths: for a fixed pairing and a fixed set of maximizers defining each simplex filtration value, the birth/death times vary smoothly with the distances. Non-differentiabilities occur only at degenerate configurations, when (i) the pairing changes, or (ii) the filtration value of a critical simplex has multiple maximizing edges. Following Solomon et al. (2022); Gameiro et al. (2016); Poulenard et al. (2018), we therefore treat the Ripser Bauer (2021) as a forward-only black box and implement a custom autograd rule, which is in the forward pass we compute persistence pairs and record the corresponding birth/death critical simplices, and in the backward pass we route gradients from each pair (b_k, d_k) to the critical edge(s) that realize these

filtration values in the distance matrix. At degenerate configurations we use an explicit subgradient selection rule, which yields a valid gradient for stochastic optimization. In addition to the non-differentiabilities of the persistence map (pairing changes and max-edge ties), our loss uses nearest-neighbor Chamfer minima and a diagonal fallback via nested $\min(\cdot)$ operators. These are piecewise-smooth and admit valid Clarke subgradients; in implementation we backpropagate through the selected nearest neighbor (and through the diagonal term when it is active), and at ties we use a deterministic uniform averaging. This yields a valid subgradient method in stochastic optimization. Solution is described in Algorithm 1.

Theorem 1 (Gradient Backpropagation via Critical-Edge Routing)**.** *Let $\mathcal{H} = \{h_1, \ldots, h_N\} \subset \mathbb{R}^C$ be the set of feature embeddings for N points and let $\mathbf{D} \in \mathbb{R}^{N\times N}$ is pairwise distance matrix where each entry is the Euclidean distance $\mathbf{D}_{ij} = \|h_i - h_j\|_2$. We construct a Vietoris-Rips filtration on these points. In this process, any simplex σ (a geometric shape like a triangle or tetrahedron) appears at a specific "time" called its filtration value $v(\sigma)$. This value is determined by the longest edge in the simplex:*

$$v(\sigma) \;=\; \max_{\{i,j\}\subset\sigma} \mathbf{D}_{ij}.$$

Let a persistent homology (PH) backend (Risper Bauer (2021)) processes this filtration and returns the multiset of topological features $\mathcal{P} = \{(b_k, d_k, \dim(k))\}_{k=1}^{K}$. Each feature k is described by: ***(i)*** *A persistence pair (b_k, d_k) representing its Birth and Death times;* ***(ii)*** *a creator simplex $\sigma_b(k)$ is the specific shape that created the feature;* ***(iii)*** *a destroyer simplex $\sigma_d(k)$ is the specific shape that destroyed (filled in) the feature.*

To make this differentiable, we identify exactly which edges determined the birth and death times. We define the Maximizer Edge Sets as:

$$E_b(k) \;:=\; \arg\max_{\{i,j\}\subset\sigma_b(k)} \mathbf{D}_{ij}, \qquad E_d(k) \;:=\; \arg\max_{\{u,v\}\subset\sigma_d(k)} \mathbf{D}_{uv}.$$

(For H_0 births, $b_k = 0$ and we take $E_b(k) = \emptyset$.)

When the filtration value of a simplex is defined by a max over its edge lengths, the gradient routes to the (edge) argmax. If the argmax is unique, the routing is unique. If several edges tie for the maximum, the function is non-smooth at that point and any Clarke subgradient is valid. Concretely, let $E_b(k)$ and $E_d(k)$ be the sets of maximizer edges for the birth and death simplices of pair k. We choose coefficients $\{\alpha_{ij}^{(k)}\}_{\{i,j\}\in E_b(k)}$ and $\{\beta_{uv}^{(k)}\}_{\{u,v\}\in E_d(k)}$ with $\alpha_{ij}^{(k)} \geq 0$ and $\sum_{\{i,j\}\in E_b(k)} \alpha_{ij}^{(k)} = 1$ (and similarly for β), and distribute the gradient across the tied edges accordingly. Common choice is uniform averaging over tied maximizers ($\alpha_{ij}^{(k)} = 1/|E_b(k)|$).

Let $\mathcal{L}$ be any loss differentiable with respect to the diagram coordinates $\{(b_k, d_k)\}$. Assume we are away from pairing-change degeneracies (i.e., the creator/destroyer simplices $\sigma_b(k), \sigma_d(k)$ are locally constant); at tie points among maximizer edges, interpret derivatives in the Clarke subgradient sense. Then a valid gradient of $\mathcal{L}$ with respect to $\mathbf{D}_{ij}$ (for $i < j$) is

$$\frac{\partial \mathcal{L}}{\partial \mathbf{D}_{ij}} = \sum_{k=1}^{K} \left(\frac{\partial \mathcal{L}}{\partial b_k}\, \alpha_{ij}^{(k)}\, \mathbb{1}_{\{\{i,j\}\in E_b(k)\}} + \frac{\partial \mathcal{L}}{\partial d_k}\, \beta_{ij}^{(k)}\, \mathbb{1}_{\{\{i,j\}\in E_d(k)\}} \right), \qquad i < j, \tag{1}$$

Where:

- $\frac{\partial \mathcal{L}}{\partial b_k}$ and $\frac{\partial \mathcal{L}}{\partial d_k}$ are the gradients from the Persistence-Weighted Chamfer Loss (PWCD) (Algorithm 3).
- $\mathbf{1}_{\{i,j\}\in E_b(k)}$ is an indicator function. It is 1 if edge $\{i, j\}$ is the Critical Creator Edge for feature k, and 0 otherwise.
- Symmetrically $\frac{\partial \mathcal{L}}{\partial \mathbf{D}_{ji}} = \frac{\partial \mathcal{L}}{\partial \mathbf{D}_{ij}}$.

Moreover, let $D_{ij} = \|h_i - h_j\|_2$ and let $g_{ij} := \partial L/\partial D_{ij}$ be accumulated for undirected edges $\{i, j\}$ with $i < j$ (as in Equation 1). For any stabilizer $\varepsilon_{\text{dist}} > 0$, a valid gradient with respect to embeddings is obtained by

summing over undirected edges: for each $i < j$,

$$\frac{\partial L}{\partial h_i} \mathrel{+}= g_{ij} \frac{h_i - h_j}{D_{ij} + \varepsilon_{\text{dist}}}, \qquad \frac{\partial L}{\partial h_j} \mathrel{-}= g_{ij} \frac{h_i - h_j}{D_{ij} + \varepsilon_{\text{dist}}}.$$

In practice, Algorithm 4 computes $(\partial L/\partial b_k, \partial L/\partial d_k)$ for PWCD, and Algorithm 1 implements Equation 1 by routing these diagram gradients to the critical edges of the paired simplices, thereby obtaining $\partial L/\partial D$ and finally $\partial L/\partial F$.

3.2.2 Persistence-Weighted Chamfer Distance

While the Differentiable Rips Filtration allows us to extract persistence diagrams, comparing them during training presents a unique challenge. Standard topological metrics like the Wasserstein distance (W_p) or Bottleneck distance (W_∞) rely on optimal transport (matching), which is computationally expensive ($O(n^3)$) and often creates sparse, unstable gradients.

A naive alternative is the Chamfer Distance, which is computationally efficient ($O(n^2)$) and differentiable. However, the standard Chamfer distance has a fatal flaw in knowledge distillation: it treats all target features equally. A Teacher's persistence diagram often contains hundreds of low-persistence features (dots near the diagonal) caused by minor fluctuations or sampling noise in the teacher's latent space. In a standard Chamfer calculation, the Student would be forced to allocate representational capacity to replicate this noise, leading to overfitting of the teacher's artifacts rather than its semantic geometry.

We solve this by introducing a Persistence-Weighted Chamfer Distance. This metric effectively functions as a soft attention mechanism. It forces the Student to prioritize robust topological features (like loops and clusters) while permitting it to ignore the Teacher's stochastic noise.

Definition. Let $P^T = \{p_i\}_{i=1}^M$ and $P^S = \{q_j\}_{j=1}^N$ be the multisets of finite persistence pairs in a fixed homology dimension, where $p = (b, d) \in \mathbb{R}^2$. Define persistence $\text{pers}(p) = d - b$, teacher weights $w(p) = \log(1 + \text{pers}(p))$, and the stabilized normalizer $\bar{w}_T = \sum_{p \in D^T} w(p) + \epsilon$. Let the squared distance to the diagonal be $\text{dist}_\Delta^2(b, d) = (d - b)^2/2$.

The Persistence-Weighted Chamfer Distance $\mathcal{L}_{CD}^w$ is defined as:

$$\mathcal{L}_{\text{topo}}(P^T, P^S) = \frac{1}{\bar{w}_T} \sum_{p \in P^T} w(p) \min\Big(\min_{q \in P_S} \|p - q\|_2^2,\ \text{dist}_\Delta^2(p) \Big) \tag{2}$$

$$+ \frac{1}{|P^S|} \sum_{q \in P^S} \min\Big(\min_{p \in D_T} \|q - p\|_2^2,\ \text{dist}_\Delta^2(q) \Big), \tag{3}$$

with the standard conventions that if $D^S = \emptyset$ then $\min_{q \in D_S}(\cdot) = +\infty$ and the precision term is 0, and if $D^T = \emptyset$ then the recall term is 0. This yields a well-defined objective for all (D^T, D^S) and ensures that unmatched student features are penalized by moving them toward the diagonal (vanishing persistence).

Theoretical Justification (See Appendix A.3).

3.3 Saliency Aware Feature Alignment

Standard feature distillation treats all spatial locations equally, often causing the student to waste representational capacity on task irrelevant background regions rather than semantic boundaries. To address this, we introduce a Saliency Aware Feature Alignment mechanism. We interpret the gradient of the task loss $\mathcal{L}_{\text{seg}}$ with respect to feature maps as a proxy for semantic importance, prioritizing regions where model predictions are most sensitive to feature perturbations.

3.3.1 Discriminative Channel Weighting

Let $F^l \in \mathbb{R}^{N \times C}$ denote the feature activations at layer l. We define the task sensitivity of the k-th channel as the global magnitude of its gradient with respect to the segmentation loss.

Although the teacher model's parameters are frozen during distillation, we explicitly compute the gradients of the task loss $\mathcal{L}_{\text{seg}}$ with respect to the *feature activations* (hidden states) to quantify spatial sensitivity. The channel-wise importance weight ω_l^k is computed as:

$$\omega_k^l = \frac{1}{N} \sum_{i=1}^{N} \left| \frac{\partial \mathcal{L}_{\text{seg}}(Y, Y_{GT})}{\partial F_{i,k}^l} \right| \tag{4}$$

where Y_{GT} denotes the ground truth labels. This step identifies which feature channels are causally responsible for the correct classification, independent of the model's weight updates.

3.3.2 Spatial Attention Transfer

We construct a spatial saliency map $M^l \in \mathbb{R}^N$ by aggregating the weighted feature responses across the channel dimension. This aggregation collapses the feature descriptors into a scalar attention score for each point, rendering the representation dimension agnostic:

$$M_i^l = \sum_{k=1}^{C} \left| \omega_k^l F_{i,k}^l \right|. \tag{5}$$

Since the teacher and student possess different channel dimensions ($C_T \neq C_S$), the raw magnitudes of their attention maps are not directly comparable. To ensure scale invariance, we apply min max normalization to generate the final attention descriptor $\hat{M}^l$:

$$\hat{M}^l = \frac{M^l - \min(M^l)}{\max(M^l) - \min(M^l) + \epsilon}. \tag{6}$$

The alignment objective minimizes the L_1 distance between the normalized attention maps of the teacher ($\hat{M}_T$) and student ($\hat{M}_S$):

$$\mathcal{L}_{\text{grad}} = \frac{1}{N} \sum_{l=1}^{L} \left\| \hat{M}_T^l - \hat{M}_S^l \right\|_1. \tag{7}$$

By optimizing $\mathcal{L}_{\text{grad}}$, we force the student to replicate the teacher's *spatial focus*, ensuring that limited capacity is allocated to the most discriminative points in the cloud regardless of the underlying feature dimension.

3.4 Optimization Objective

To complement the geometric and spatial alignment provided by the topological and saliency modules, we incorporate a Semantic Distillation term using Kullback-Leibler Divergence (KLD) Kullback (1951). While $\mathcal{L}_{\text{topo}}$ and $\mathcal{L}_{\text{grad}}$ align the encoder's latent manifold, the KLD loss is applied to the temperature-scaled output logits of the classifier. This guides the student to mimic not only the teacher's hard predictions but also the underlying class probability distribution, capturing inter-class correlations.

The total training objective integrates the standard segmentation task with the three distillation constraints:

$$\mathcal{L}_{\text{total}} = \mathcal{L}_{\text{seg}} + \lambda_{\text{topo}}\mathcal{L}_{\text{topo}} + \lambda_{\text{grad}}\mathcal{L}_{\text{grad}} + \lambda_{\text{kd}}\mathcal{L}_{\text{kd}}, \tag{8}$$

where:

- $\mathcal{L}_{\text{seg}}$ is the standard Cross-Entropy loss for point-wise classification using ground truth labels.
- $\mathcal{L}_{\text{topo}}$ enforces the preservation of high-level topological structures (clusters and loops) in the latent space.
- $\mathcal{L}_{\text{grad}}$ ensures the student focuses on the same discriminative spatial regions as the teacher.
- $\mathcal{L}_{\text{kd}}$ minimizes the KL divergence between the teacher's and student's softened logits, transferring semantic confidence.

The hyperparameters λ_{topo}, λ_{grad}, and λ_{kd} balance the contribution of each knowledge stream.

4 Experiments and Results

To assess our topology-aware distillation framework, we performed experiments on three prominent autonomous driving datasets: SemanticKITTI Behley et al. (2019), Waymo Open Dataset Caesar et al. (2020), and NuScenes Sun et al. (2020). These datasets offer large-scale, real-world point-cloud sequences, ideal for benchmarking point-cloud processing techniques. We provide detailed descriptions of datasets, training protocols, and evaluation procedures in the Appendix C.

4.1 Experimental Results

Performance on nuScenes Dataset. Table 1 compares our method against state-of-the-art frameworks on the nuScenes test set. While recent cross-modal methods integrating camera data (LC), such as TPV-IGKD Li et al. (2024a) (81.3% mIoU) and U2MKD Liu & et al. (2024) (81.2% mIoU), establish the current upper bound, our proposed LiDAR-only student achieves a highly competitive 78.2% mIoU. This significantly outperforms established baselines including Cylinder3D Zhu et al. (2021) (76.1%), AMVNet Liong et al. (2020) (76.1%), and 2DPASS Yan et al. (2022) (76.2%). The advantages of our approach are further highlighted by its class-wise performance. Notably, our student achieves the highest accuracy among all compared models including multi-modal fusion ones in the car (94.3%) category and demonstrates superior performance in the terrain (89.3%) category. This suggests that while camera-based methods rely on visual texture, which can be inconsistent for ground surfaces, our Persistence-Weighted Topological Loss effectively maintains the structural integrity of large geometric manifolds like terrain. Furthermore, the gradient-guided alignment sharpens object boundaries, allowing our lightweight student to resolve the complex geometry of cars better than heavier fusion models.

Methods	**mIoU**	barrier	bicycle	bus	car	construction	motorcycle	pedestrian	traffic-cone	trailer	truck	driveable	other	sidewalk	terrain	manmade	vegetation
RangeNet++ Milioto et al. (2019)	65.5	66.0	21.3	77.2	80.9	30.2	66.8	69.6	52.1	54.2	72.3	94.1	66.6	63.5	70.1	83.1	79.8
PolarNet Zhang et al. (2020b)	71.0	74.7	28.2	85.3	90.9	35.1	77.5	71.3	58.8	57.4	76.1	96.5	71.1	74.7	74.0	87.3	85.7
SalsaNext Cortinhal et al. (2020b)	72.2	74.8	34.1	85.9	88.4	42.2	72.4	72.2	63.1	61.3	76.5	96.0	70.8	71.2	71.5	86.7	84.4
Cylinder3D Zhu et al. (2021)	76.1	76.4	40.3	91.2	93.8	51.3	78.0	78.9	64.9	62.1	84.4	96.8	71.6	76.4	75.4	90.5	87.4
C3D_0.5× + KA Hou et al. (2022b)	73.9	74.2	36.3	88.5	87.6	47.1	76.9	78.3	63.5	57.6	83.4	94.9	70.3	73.8	73.2	88.4	86.3
AMVNet Liong et al. (2020)	76.1	79.8	32.4	87.4	90.4	**62.5**	81.9	75.3	**72.3**	**83.5**	65.1	97.4	67.0	78.8	74.6	90.8	87.9
2DPASS Yan et al. (2022)	76.2	75.3	43.5	95.3	91.2	54.5	78.9	78.2	62.1	70.0	84.2	96.3	73.2	74.2	74.9	89.8	85.9
SDSeg3D Li et al. (2022)	77.7	77.5	49.4	93.9	92.5	54.9	86.7	80.1	67.8	65.7	**86.0**	96.4	74.0	74.9	74.5	86.0	82.8
RPVNet Xu et al. (2021)	77.6	78.2	43.4	92.7	93.2	49.0	85.7	80.6	66.9	69.4	80.5	96.9	73.5	75.9	76.0	90.6	88.9
GFNet Qiu et al. (2022)	76.1	**81.1**	31.6	76.0	90.5	60.2	80.7	75.3	71.8	82.5	65.1	**97.8**	**80.4**	80.4	76.2	**91.8**	88.9
SVASeg Zhao et al. (2022)	74.7	74.1	44.5	88.4	86.6	48.2	72.4	72.3	61.3	57.5	75.7	96.3	70.7	74.7	74.6	87.3	86.9
U2MKD Liu & et al. (2024) (LC)	81.2	85.9	43.4	93.1	90.1	72.5	86.3	81.6	78.5	85.7	76.5	97.6	69.8	80.3	77.0	91.8	89.5
KT-Weakly Wang et al. (2025)(LC)	80.2	-	-	-	-	-	-	-	-	-	-	-	-	-	-	-	-
MV3Dseg Sun et al. (2025)	81.1	79.7	**59.2**	**96.0**	92.6	60.3	**88.4**	**83.6**	70.8	80.2	81.8	96.7	74.4	**79.6**	76.1	90.0	88.2
TPV-IGKD Li et al. (2024a) (LC)	**81.3**	85.4	43.2	92.9	93.2	75.7	77.4	83.4	77.2	86.8	77.4	97.7	71.4	81.3	77.4	91.7	89.0
Student w.o KD	76.1	76.1	46.7	89.9	92.2	40.4	83.9	78.3	63.2	68.2	81.8	96.3	72.8	73.6	75.4	89.7	88.8
Student with KD	78.2	79.1	48.3	92.9	**94.3**	41.3	85.7	82.9	62.4	70.2	80.3	96.7	76.3	74.2	**78.8**	90.9	**89.3**

Table 1: Comparison of our proposed method with previous state-of-the-art LiDAR semantic segmentation methods on the nuScenes test dataset. The table reports the mean Intersection over Union (mIoU) for different models across various object categories.

Performance on SemanticKITTI. Table 2 details the semantic segmentation performance on the SemanticKITTI test set. Our distilled student model achieves a highly competitive 73.1% mIoU, effectively approaching the state-of-the-art MV3Dseg Sun et al. (2025) (73.2%) while using a significantly lighter architecture. Crucially, our method outperforms recent complex baselines such as KT-Weakly Wang et al. (2025) (71.4%) and C3D+SCPNet Xia et al. (2023) (71.5%). The efficacy of our distillation strategy is evidenced by a substantial 1.6% improvement over the baseline student (71.5%). Theoretical advantages of

our Topology-Aware Distillation become evident in the class-wise breakdown. While multi-view methods like MV3Dseg excel in texture-heavy classes (e.g., vegetation), our approach dominates in geometrically complex and structural categories. This confirms that while Scene Completion methods (e.g., SCPNet) tend to over-smooth fine details to fill occlusions, our persistence-based loss (H_0, H_1) forces the student to preserve thin, disconnected topological features and complex loops, effectively preventing the washing out of small objects common in lightweight networks.

Methods	mIoU	car	bicycle	motorcycle	truck	other-vehicle	person	bicyclist	motorcyclist	road	parking	sidewalk	other-ground	building	fence	vegetation	trunk	terrain	pole	traffic
SalsaNext Cortinhal et al. (2020b)	59.5	91.9	48.3	38.6	38.9	31.9	60.2	59.0	19.4	91.7	63.7	75.8	29.1	90.2	64.2	81.8	63.6	66.5	54.3	47.4
KPConv Thomas et al. (2019)	58.8	96.0	32.0	42.5	33.4	44.3	61.5	61.6	11.8	88.8	61.3	72.7	31.6	**95.0**	64.2	84.8	69.2	69.1	56.4	47.4
FusionNet Zhang et al. (2020a)	61.3	95.3	47.5	37.7	41.8	34.5	59.5	56.8	11.9	91.8	68.7	77.1	30.5	90.5	69.4	84.5	69.8	68.5	60.4	46.2
KPRNet Kochanov et al. (2020)	63.1	95.5	54.1	47.9	23.6	42.6	65.9	65.0	16.5	93.2	73.9	80.6	30.2	91.7	64.8	85.7	69.8	71.2	58.7	64.1
TORNADONet Gerdzhev et al. (2021)	63.1	94.2	51.2	48.1	40.0	38.2	63.6	60.1	34.9	89.7	66.7	74.5	28.7	91.3	65.8	85.6	71.5	70.1	58.0	49.2
SPVNAS Tang et al. (2020)	66.4	97.3	51.5	50.8	**59.8**	58.8	65.7	62.5	43.7	90.2	67.6	75.2	16.9	91.3	65.9	86.1	73.4	71.0	64.6	66.9
Cylinder3D Zhu et al. (2021)	68.9	97.1	67.6	50.8	50.8	58.5	73.7	69.2	48.0	92.2	65.0	77.0	32.3	90.7	66.5	85.6	72.5	69.8	62.4	66.2
PolarNet+M2S-KD Qiu et al. (2023)	58.0	93.5	45.9	36.3	27.6	34.9	55.0	51.4	15.8	91.1	64.7	73.8	26.1	92.5	67.0	84.6	63.4	67.4	50.7	59.5
C3D+M2S-KD Qiu et al. (2023)	65.6	96.4	60.8	54.8	42.8	51.2	69.1	67.8	34.8	92.2	66.5	76.7	30.4	91.1	65.7	85.5	69.8	68.6	60.7	61.0
C3D+SCPNet Xia et al. (2023)	71.5	97.5	60.9	56.3	58.6	**65.9**	70.7	71.8	58.7	93.6	72.1	80.9	36.2	**93.3**	**72.1**	86.2	74.1	71.6	66.7	**71.8**
U2MKD Liu & et al. (2024) (LC)	69.6	-	-	-	-	-	-	-	-	-	-	-	-	-	-	-	-	-	-	-
TPV-IGKD Li et al. (2024a)	69.3	96.7	63.3	65.8	54.6	63.1	76.5	**80.7**	41.6	90.0	60.3	75.4	29.1	91.1	66.3	85.9	74.2	70.3	63.8	69.1
KT-Weakly Wang et al. (2025)(LC)	71.4	-	-	-	-	-	-	-	-	-	-	-	-	-	-	-	-	-	-	-
MV3Dseg Sun et al. (2025)	**73.2**	97.6	69.8	**76.1**	**65.4**	61.3	**79.1**	80.0	**71.1**	**94.2**	67.6	78.6	37.5	91.8	65.9	85.7	72.8	73.7	63.5	60.0
Student w.o KD	71.5	96.0	71.0	56.5	56.5	62.2	77.2	72.8	56.8	95.5	68.7	80.5	36.4	94.0	70.1	89.0	76.0	73.4	66.1	69.8
Student with KD	73.1	96.8	**72.6**	58.8	58.8	65.1	77.6	73.9	56.5	92.8	**70.5**	**80.3**	**43.6**	91.6	71.7	**87.4**	**76.6**	**74.4**	**68.3**	71.6

Table 2: Comparison of semantic segmentation performance on the SemanticKITTI dataset. The table reports the mean Intersection over Union (mIoU) for different models across various object categories.

We further evaluate our framework on the Waymo Open Dataset, as summarized in Table 4. Among multi-modal methods utilizing both LiDAR and camera (LC), MSeg3D Li et al. (2023) and UMKD (B) Sun et al. (2024) demonstrate strong performance with validation mIoU scores of 69.6 and 71.1, respectively. Within the LiDAR-only (L) category, LidarMultiNet Ye et al. (2022) achieves a leading test mIoU of 71.1; however, it should be noted that this approach relies on 3D bounding boxes as an additional supervision signal during training. Our teacher model sets a high performance ceiling for LiDAR-only methods with a test mIoU of 71.3. Notably, our distilled student model achieves a test mIoU of 69.5, making it competitive with several heavier architectures and even approaching the performance of multi-modal methods. This performance is particularly significant given the student's efficiency; as shown in Table 3, our model maintains competitive generalization while offering a substantial reduction in parameter count.

4.2 Comprehensive Teacher–Student Analysis

Tables 5 and 6 compare the Teacher (46.16M params) and Student (2.78M params) models on nuScenes, showcasing the significant efficiency benefits of our distillation framework. The Teacher model possesses 16.6× more parameters than the Student, necessitating a deeper architecture suited for high-accuracy tasks on high-end hardware. In contrast, the Student's lightweight design significantly reduces computational overhead, achieving a 36.70× reduction in encoder FLOPs. This efficiency translates to a 2.47× faster total CPU time (203.10 ms vs. 501.11 ms) and a 4.19× faster total CUDA time (102.07 ms vs. 427.31 ms), making it highly suitable for real-time applications.Additionally, the Student requires 4.5× less peak CUDA memory for matrix multiplication operations (3.57 GB vs. 16.05 GB), which allows it to benefit more effectively from Flash Attention optimizations. At the operational level, the Teacher's resource demands are markedly higher, requiring between 2.91× and 4.69× more memory for operations such as Alloc, Idx, and LN. While the Teacher provides an accuracy ceiling on high-performance hardware, the Student's drastically reduced memory footprint and accelerated execution make it ideal for deployment on resource-constrained edge devices.

Method	Params (M)	FPS
RangeNet++ Milioto et al. (2019)	50.0	12.5
PolarNet Zhang et al. (2020b)	45.0	16.7
SalsaNext Cortinhal et al. (2020b)	6.7	23.8
Cylinder3D Zhu et al. (2021)	53.0	12.0
KPConv Thomas et al. (2019)	15.0	12.0
SPVNAS Tang et al. (2020)	1.0	16.0
KT-weakly Wang et al. (2025)	-	25.0
MV3DSeg Sun et al. (2025)	45.6	22.7
U2MKD Liu & et al. (2024)	21.2	10.64
TPV-IGKD Li et al. (2024a)	146.18	8.7
PTv3 (Teacher)	46.16	16.61
Our Student	**2.78**	**27.64**

Table 3: Comparison of model size (in M parameters) and inference speed (FPS) on NuScenes.

Method	Input	mIoU (test / val)
MSeg3D Li et al. (2023)	LC	70.5 / 69.6
UMKD (B) Sun et al. (2024)	LC	70.0 / 71.1
PMF Zhuang et al. (2021)	LC	– / 58.2
SalsaNext Cortinhal et al. (2020a)	L	55.8 / –
Realsurf Sun et al. (2024)	L	67.6 / –
SPVCNN++ Tang et al. (2020)	L	67.7 / –
VueNet3D Sun et al. (2024)	L	68.6 / –
SphereFormer Lai et al. (2023)	L	– / 69.9
LidarMultiNet Ye et al. (2022)	L	71.1 / 69.9
Ours (Student w/o KD)	L	67.2 / 66.5
Ours (Student w/ KD)	L	**69.5** / **68.7**
Ours (Teacher)	L	71.3 / 69.8

Table 4: Semantic segmentation mIoU on Waymo Open Dataset. Inputs: LiDAR (L), Camera (C).

Metric	Teacher (46.16M)	Student (2.78M)	Comparison
Total Parameters	46,160,000 (∼46.16M)	2,780,000 (∼2.78M)	Student is 16.6× smaller
Encoder Depths	(2, 2, 2, 6, 2)	(1, 1, 1, 2, 1)	2.33× fewer blocks
Encoder Channels	(32, 64, 128, 256, 512)	(16, 16, 32, 64, 128)	2–4× smaller
Encoder Attention Heads	(2, 4, 8, 16, 32)	(1, 1, 2, 4, 8)	2–4× fewer
Decoder Depths	(2, 2, 2, 2)	(1, 1, 1, 1)	2× fewer blocks
Decoder Channels	(64, 64, 128, 256)	(64, 64, 128, 128)	Last stage is 2× smaller
Decoder Attention Heads	(4, 4, 8, 16)	(2, 2, 4, 8)	2× fewer
Patch Size	1024	1024	Same
Encoder GFLOPs	380.25	10.36	36.7× lower
Decoder GFLOPs	116.44	33.45	3.48× lower
Attention Compute (Encoder)	22.58	0.60	37.63× lower
Inference Time (excl. overhead)	∼0.0592 s	∼0.0362 s	1.64× faster
Batch Inference Time	∼7.34 s	∼4.38 s	Student faster
FPS	∼16.9	∼27.7	≈ 1.64× higher
Fixed Overhead	∼0.018 s	∼0.011 s	≈ 1.64× faster
Attention Mechanism	Flash Attention	Flash Attention	Student benefits more

Table 5: Comparison of Teacher and Student models on NuScenes.

4.3 Effectiveness of Individual Loss Components

Table 7 demonstrates the effectiveness of each proposed loss component. Adding the topology-awareness loss $\mathcal{L}_{\text{topo}}$ to the baseline ($\mathcal{L}_{\text{seg}}$+$\mathcal{L}_{\text{KLD}}$) improves mIoU by +1.1 on SemanticKITTI (71.5 → 72.6), +1.5 on Waymo (69.2 → 70.7), and +0.7 on nuScenes (76.9 → 77.6), indicating that preserving global geometric structure consistently benefits cross-dataset generalization. Meanwhile, the gradient-guided alignment loss $\mathcal{L}_{\text{grad}}$ yields consistent gains of +0.8, +1.0, and +0.3 on SemanticKITTI, Waymo, and nuScenes respectively, suggesting improved refinement of locally discriminative features. Combining $\mathcal{L}_{\text{topo}}$ and $\mathcal{L}_{\text{grad}}$ achieves the best results on all benchmarks, reaching 73.1 (SemanticKITTI), 71.5 (Waymo), and 78.1 (nuScenes), confirming their complementary contributions.

5 Conclusion and Future Work

We presented a novel distillation framework that bridges the gap between high-capacity 3D perception models and resource-constrained deployment environments. By integrating Topological Distillation with Saliency-Aware Feature Alignment, our method enables a lightweight student model to inherit not only the semantic precision of a teacher but also its underlying geometric manifold structure.

Metric	Teacher	Student	Improvement
Total CPU Time[b]	501.11 ms	203.10 ms	2.47× faster
Total CUDA Time	427.31 ms	102.07 ms	4.19× faster
MM_{add} (CUDA Mem)[a]	16.05 GB	3.57 GB	4.5× less
MM_{add} (Self CUDA)[a]	173.51 ms	34.75 ms	5.0× faster
Alloc (CUDA Memory)	8.73 GB	3.00 GB	2.91× less
Idx (CUDA Memory)	7.27 GB	1.78 GB	4.08× less
GELU (CUDA Memory)	6.82 GB	1.67 GB	4.08× less
LN (CUDA Memory)[a]	4.62 GB	985.43 MB	4.69× less
Infer (Self CPU Time)	47.01 ms	37.24 ms	1.26× faster
MM_{add} (Self CPU Time)[a]	5.40 ms	2.72 ms	1.99× faster

[a] Attention-related ops: matrix multiplications for Q, K, V and layer normalization.
[b] Total CPU time is from a profiling run; separate memory-focused run shows 3.02× ratio (Teacher: 278.80 ms, Student: 92.44 ms).

Table 6: Comparison of memory and time usage between Teacher and Student.

$\mathcal{L}_{\text{KLD}}$	$\mathcal{L}_{\text{seg}}$	$\mathcal{L}_{\text{topo}}$	$\mathcal{L}_{\text{grad}}$	S.KITTI	Waymo	nuScenes
✓	✓			71.8	67.9	76.9
✓	✓	✓		72.6	68.7	77.6
✓	✓		✓	72.3	68.2	77.2
✓	✓	✓	✓	**73.1**	**69.5**	**78.1**

Table 7: Influence of each loss component on the final performance (mIoU %).

Extensive experiments on nuScenes, SemanticKITTI, and Waymo demonstrate that our approach achieves state-of-the-art performance among LiDAR-based distillation methods. Specifically, our student model retains competitive segmentation accuracy while delivering a 16× reduction in parameters and up to 1.9× acceleration in inference speed. Crucially, our qualitative analysis reveals that enforcing topological consistency effectively mitigates the fragmentation common in lightweight networks, ensuring robust performance on complex, large-scale structures.

Future Work. Although our topology-preserving subsampling substantially reduces the cost of persistent-homology computation during training, a natural next step is to replace heuristic selection with learnable, task-adaptive topological token sampling and amortized PH computation, enabling larger filtrations and higher-order homology under the same budget. A second direction is extending topology- and gradient-guided distillation to spatio-temporal perception and multi-parameter topology, enforcing consistency across multi-sweep sequences and across geometric scales. Finally, we will study topology-aware distillation in cross-modal and open-world settings, distilling structural priors from camera/BEV and vision(-language) foundation models into deployment-oriented backbones (e.g., hardware-optimized attention or linear-time state-space models) to improve long-tail generalization and robustness under missing or misaligned modalities.

References

Ulrich Bauer. Ripser: efficient computation of Vietoris-Rips persistence barcodes. *J. Appl. Comput. Topol.*, 5 (3):391–423, 2021. ISSN 2367-1726. doi: 10.1007/s41468-021-00071-5. URL https://doi.org/10.1007/s41468-021-00071-5.

Jens Behley, Martin Garbade, Andres Milioto, Jonas Quenzel, Sven Behnke, Cyrill Stachniss, and Jurgen Gall. Semantickitti: A dataset for semantic scene understanding of lidar sequences. *Proceedings of the IEEE International Conference on Computer Vision (ICCV)*, pp. 9297–9307, 2019.

Rickard Brüel-Gabrielsson, Bradley J Nelson, Anjan Dwaraknath, and Primoz Skraba. A topology layer for machine learning. In *International Conference on Artificial Intelligence and Statistics (AISTATS)*, pp. 1553–1563, 2020.

Holger Caesar, Alex Bankiti, Alexander H Lang, Sourabh Vora, Venice Erin Liong, Qiang Xu, Anush Krishnan, Yu Pan, Giancarlo Baldan, and Oscar Beijbom. nuscenes: A multimodal dataset for autonomous driving. *Proceedings of the IEEE Conference on Computer Vision and Pattern Recognition (CVPR)*, pp. 11621–11631, 2020.

Chao Cao, Marius Preda, and Titus Zaharia. 3d point cloud compression: A survey. In *Proceedings of the 24th International Conference on 3D Web Technology*, Web3D '19, pp. 1–9, New York, NY, USA, 2019. Association for Computing Machinery. ISBN 9781450367981. doi: 10.1145/3329714.3338130. URL https://doi.org/10.1145/3329714.3338130.

Mathieu Carrière, Frédéric Chazal, Yuichi Ike, Théo Lacombe, Martin Royer, and Yuhei Umeda. Perslay: A neural network layer for persistence diagrams and new graph topological signatures. In *International Conference on Artificial Intelligence and Statistics*, pp. 2786–2796. PMLR, 2020.

Jun Cen, Shiwei Zhang, Yixuan Pei, Kun Li, Hang Zheng, Maochun Luo, Yingya Zhang, and Qifeng Chen. Cmdfusion: Bidirectional fusion network with cross-modality knowledge distillation for lidar semantic segmentation. *IEEE Robotics and Automation Letters*, 9(1):771–778, 2024. doi: 10.1109/LRA.2023.3335771.

Xiaozhi Chen, Huimin Ma, Ji Wan, Bo Li, and Tian Xia. Multi-view 3d object detection network for autonomous driving. In *Proceedings of the IEEE conference on Computer Vision and Pattern Recognition*, pp. 1907–1915, 2017.

Jungwook Choi, Swagath Venkataramani, Vijayalakshmi (Viji) Srinivasan, Kailash Gopalakrishnan, Zhuo Wang, and Pierce Chuang. Accurate and efficient 2-bit quantized neural networks. In A. Talwalkar, V. Smith, and M. Zaharia (eds.), *Proceedings of Machine Learning and Systems*, volume 1, pp. 348–359, 2019. URL https://proceedings.mlsys.org/paper_files/paper/2019/file/c443e9d9fc984cda1c5cc447fe2c724d-Paper.pdf.

Christopher Choy, JunYoung Gwak, and Silvio Savarese. 4d spatio-temporal convnets: Minkowski convolutional neural networks. In *Proceedings of the IEEE/CVF conference on computer vision and pattern recognition*, pp. 3075–3084, 2019.

David Cohen-Steiner, Herbert Edelsbrunner, and John Harer. Stability of persistence diagrams. *Discrete & Computational Geometry*, 37(1):103–120, 2007. doi: 10.1007/s00454-006-1276-5.

Tiago Cortinhal, George Tzelepis, and Eren Erdal Aksoy. SalsaNext: Fast, Uncertainty-Aware Semantic Segmentation of LiDAR Point Clouds. In *Advances in Visual Computing: 15th International Symposium, ISVC 2020, San Diego, CA, USA, October 5–7, 2020, Proceedings, Part II*, volume 12510 of *Lecture Notes in Computer Science*, pp. 207–222. Springer, 2020a.

Tiago Cortinhal, George Tzelepis, and Eren Erdal Aksoy. Salsanext: Fast, uncertainty-aware semantic segmentation of lidar point clouds. In *Advances in Visual Computing: 15th International Symposium, ISVC 2020, San Diego, CA, USA, October 5–7, 2020, Proceedings, Part II 15*, pp. 207–222. Springer, 2020b.

Runpei Dong, Zhanhong Tan, Mengdi Wu, Linfeng Zhang, and Kaisheng Ma. Finding the task-optimal low-bit sub-distribution in deep neural networks. In *International Conference on Machine Learning*, pp. 5343–5359. PMLR, 2022.

Marcio Gameiro, Yasuaki Hiraoka, and Ippei Obayashi. Continuation of point clouds via persistence diagrams. *Physica D: Nonlinear Phenomena*, 334:118–132, 2016. doi: 10.1016/j.physd.2016.03.011.

Andreas Geiger, Philip Lenz, and Raquel Urtasun. Are we ready for autonomous driving? the kitti vision benchmark suite. In *2012 IEEE conference on computer vision and pattern recognition*, pp. 3354–3361. IEEE, 2012.

Martin Gerdzhev, Ryan Razani, Ehsan Taghavi, and Liu Bingbing. Tornado-net: multiview total variation semantic segmentation with diamond inception module. In *2021 IEEE International Conference on Robotics and Automation (ICRA)*, pp. 9543–9549. IEEE, 2021.

Tim Golla and Reinhard Klein. Real-time point cloud compression. In *2015 IEEE/RSJ International Conference on Intelligent Robots and Systems (IROS)*, pp. 5087–5092, 2015. doi: 10.1109/IROS.2015.7354093.

Ruben Gomez-Ojeda, Jesus Briales, and Javier Gonzalez-Jimenez. Pl-svo: Semi-direct monocular visual odometry by combining points and line segments. In *2016 IEEE/RSJ International Conference on Intelligent Robots and Systems (IROS)*, pp. 4211–4216. IEEE, 2016.

Meng-Hao Guo, Jun-Xiong Cai, Zheng-Ning Liu, Tai-Jiang Mu, Ralph R Martin, and Shi-Min Hu. Pct: Point cloud transformer. *Computational Visual Media*, 7:187–199, 2021a.

Xiaoyang Guo, Shaoshuai Shi, Xiaogang Wang, and Hongsheng Li. Liga-stereo: Learning lidar geometry aware representations for stereo-based 3d detector. In *Proceedings of the IEEE/CVF international conference on computer vision*, pp. 3153–3163, 2021b.

Sangchul Hahn and Heeyoul Choi. Self-knowledge distillation in natural language processing. In *Proceedings of the International Conference on Recent Advances in Natural Language Processing (RANLP)*, pp. 423–430, 2019. doi: 10.26615/978-954-452-056-4_050. URL https://aclanthology.org/R19-1050/.

Dan Halperin and Niklas Eisl. Point cloud based scene segmentation: A survey, 2025. URL https://arxiv.org/abs/2503.12595.

Song Han, Huizi Mao, and William J. Dally. Deep compression: Compressing deep neural networks with pruning, trained quantization and huffman coding. In *Proceedings of the International Conference on Learning Representations (ICLR)*, 2016. URL https://arxiv.org/abs/1510.00149.

Haoyu He, Xingjian Shi, Jonas Mueller, Sheng Zha, Mu Li, and George Karypis. Distiller: A systematic study of model distillation methods in natural language processing. In *Proceedings of the Second Workshop on Simple and Efficient Natural Language Processing*, pp. 119–133, Virtual, 2021. Association for Computational Linguistics. doi: 10.18653/v1/2021.sustainlp-1.13. URL https://aclanthology.org/2021.sustainlp-1.13/.

Geoffrey Hinton, Oriol Vinyals, and Jeff Dean. Distilling the knowledge in a neural network. In *Advances in Neural Information Processing Systems (NeurIPS)*, pp. 1–2, 2014.

Geoffrey Hinton, Oriol Vinyals, and Jeff Dean. Distilling the knowledge in a neural network. *arXiv preprint arXiv:1503.02531*, 2015.

Yuenan Hou, Xinge Zhu, Yuexin Ma, Chen Change Loy, and Yikang Li. Point-to-voxel knowledge distillation for lidar semantic segmentation. In *Proceedings of the IEEE/CVF Conference on Computer Vision and Pattern Recognition (CVPR)*, pp. 8479–8488, June 2022a.

Yuenan Hou, Xinge Zhu, Yuexin Ma, Chen Change Loy, and Yikang Li. Point-to-voxel knowledge distillation for lidar semantic segmentation. In *Proceedings of the IEEE/CVF conference on computer vision and pattern recognition*, pp. 8479–8488, 2022b.

Yuenan Hou, Xinge Zhu, Yuexin Ma, Chen Change Loy, and Yikang Li. Point-to-voxel knowledge distillation for lidar semantic segmentation. In *Proceedings of the IEEE/CVF conference on computer vision and pattern recognition*, pp. 8479–8488, 2022c.

Andrew Howard, Mark Sandler, Grace Chu, Liang-Chieh Chen, Bo Chen, Mingxing Tan, Weijun Wang, Yukun Zhu, Ruoming Pang, Vijay Vasudevan, et al. Searching for mobilenetv3. In *Proceedings of the IEEE/CVF international conference on computer vision*, pp. 1314–1324, 2019.

Xiaoling Hu, Fuxin Li, Dimitris Samaras, and Chao Chen. Topology-preserving deep image segmentation. In *Advances in neural information processing systems (NeurIPS)*, volume 32, 2019.

Eun Som Jeon, Rahul Khurana, Aishani Pathak, and Pavan Turaga. Leveraging topological guidance for improved knowledge distillation. In *Proceedings of the ICML 2024 Workshop on Geometry-grounded Representation Learning and Generative Modeling*, 2024. URL https://arxiv.org/abs/2407.05316.

Jungeun Kim, Junwon You, Dongjin Lee, Ha Young Kim, and Jae-Hun Jung. Do topological characteristics help in knowledge distillation? In *Forty-first International Conference on Machine Learning*, 2024. URL https://openreview.net/forum?id=2dEH0u8w0b.

Deyvid Kochanov, Fatemeh Karimi Nejadasl, and Olaf Booij. Kprnet: Improving projection-based lidar semantic segmentation. *arXiv preprint arXiv:2007.12668*, 2020.

Solomon Kullback. Kullback-leibler divergence, 1951.

Xin Lai, Yukang Chen, Fanbin Lu, Jianhui Liu, and Jiaya Jia. Spherical transformer for lidar-based 3d recognition. In *Proceedings of the IEEE/CVF Conference on Computer Vision and Pattern Recognition (CVPR)*, pp. 17545–17555, 2023.

Alex H Lang, Sourabh Vora, Holger Caesar, Lubing Zhou, Jiong Yang, and Oscar Beijbom. Pointpillars: Fast encoders for object detection from point clouds. In *Proceedings of the IEEE/CVF conference on computer vision and pattern recognition*, pp. 12697–12705, 2019.

Bo Li, Tianlei Zhang, and Tian Xia. Vehicle detection from 3d lidar using fully convolutional network. In *Proceedings of Robotics: Science and Systems (RSS)*, 2016. doi: 10.15607/RSS.2016.XII.042. URL https://www.roboticsproceedings.org/rss12/p42.pdf.

Jia-Chen Li, Jun-Guo Lu, Ming Wei, Hong-Yi Kang, and Qing-Hao Zhang. Tpv-igkd: Image-guided knowledge distillation for 3d semantic segmentation with tri-plane-view. *IEEE Transactions on Intelligent Transportation Systems*, 25(8):10405–10416, 2024a.

Jia-Chen Li, Jun-Guo Lu, Ming Wei, Hong-Yi Kang, and Qing-Hao Zhang. Tpv-igkd: Image-guided knowledge distillation for 3d semantic segmentation with tri-plane-view. *IEEE Transactions on Intelligent Transportation Systems*, 25(8):10405–10416, 2024b. doi: 10.1109/TITS.2024.3361163.

Jiale Li, Hang Dai, and Yong Ding. Self-distillation for robust lidar semantic segmentation in autonomous driving. In *European conference on computer vision*, pp. 659–676. Springer, 2022.

Jiale Li, Hang Dai, Hao Han, and Yong Ding. Mseg3d: Multimodal 3d semantic segmentation for autonomous driving. In *Proceedings of the IEEE/CVF Conference on Computer Vision and Pattern Recognition (CVPR)*, pp. 21694–21704, 2023.

Venice Erin Liong, Thi Ngoc Tho Nguyen, Sergi Widjaja, Dhananjai Sharma, and Zhuang Jie Chong. Amvnet: Assertion-based multi-view fusion network for lidar semantic segmentation. *CoRR*, abs/2012.04934, 2020. URL https://arxiv.org/abs/2012.04934.

Y. Liu and et al. Uni-to-multi modal knowledge distillation for bidirectional lidar-camera semantic segmentation. *IEEE Transactions on Pattern Analysis and Machine Intelligence (TPAMI)*, PP(99):1–14, 2024.

Yifan Liu, Ke Chen, Chris Liu, Zengchang Qin, Zhenbo Luo, and Jingdong Wang. Structured knowledge distillation for semantic segmentation. In *Proceedings of the IEEE/CVF conference on computer vision and pattern recognition*, pp. 2604–2613, 2019a.

Zechun Liu, Haoyuan Mu, Xiangyu Zhang, Zichao Guo, Xin Yang, Kwang-Ting Cheng, and Jian Sun. Metapruning: Meta learning for automatic neural network channel pruning. In *Proceedings of the IEEE/CVF international conference on computer vision*, pp. 3296–3305, 2019b.

Christos Louizos, Max Welling, and Diederik P. Kingma. Learning sparse neural networks through l_0 regularization. In *Proceedings of the International Conference on Learning Representations (ICLR)*, 2018. URL https://openreview.net/forum?id=H1Y8hhg0b&noteId=SkdVNJ6Bz.

Ningning Ma, Xiangyu Zhang, Hai-Tao Zheng, and Jian Sun. Shufflenet v2: Practical guidelines for efficient cnn architecture design. In *Proceedings of the European conference on computer vision (ECCV)*, pp. 116–131, 2018.

Xu Ma, Can Qin, Haoxuan You, Haoxi Ran, and Yun Fu. Rethinking network design and local geometry in point cloud: A simple residual mlp framework. In *Proceedings of the International Conference on Learning Representations (ICLR)*, 2022. URL https://openreview.net/forum?id=3Pbra-_u76D.

Andres Milioto, Ignacio Vizzo, Jens Behley, and Cyrill Stachniss. Rangenet++: Fast and accurate lidar semantic segmentation. In *2019 IEEE/RSJ international conference on intelligent robots and systems (IROS)*, pp. 4213–4220. IEEE, 2019.

Michael Moor, Max Horn, Bastian Rieck, and Karsten Borgwardt. Topological autoencoders. In *International Conference on Machine Learning (ICML)*, pp. 7045–7054, 2020.

Markus Nagel, Mart van Baalen, Tijmen Blankevoort, and Max Welling. Data-free quantization through weight equalization and bias correction. In *Proceedings of the IEEE/CVF International Conference on Computer Vision*, pp. 1325–1334, 2019.

Yong-Joo Oh and Yoshio Watanabe. Development of small robot for home floor cleaning. In *Proceedings of the 41st SICE Annual Conference. SICE 2002.*, volume 5, pp. 3222–3223. IEEE, 2002.

Adrien Poulenard, Primoz Skraba, and Maks Ovsjanikov. Topological function optimization for continuous shape matching. *Computer Graphics Forum*, 37(5):13–25, 2018.

Charles R Qi, Hao Su, Kaichun Mo, and Leonidas J Guibas. Pointnet: Deep learning on point sets for 3d classification and segmentation. In *Proceedings of the IEEE conference on computer vision and pattern recognition*, pp. 652–660, 2017.

Haibo Qiu, Baosheng Yu, and Dacheng Tao. Gfnet: Geometric flow network for 3d point cloud semantic segmentation. *arXiv preprint arXiv:2207.02605*, 2022.

Shoumeng Qiu, Feng Jiang, Haiqiang Zhang, Xiangyang Xue, and Jian Pu. Multi-to-single knowledge distillation for point cloud semantic segmentation. In *2023 IEEE International Conference on Robotics and Automation (ICRA)*, pp. 9303–9309. IEEE, 2023.

Ahmad Rashid, Vasileios Lioutas, Abbas Ghaddar, and Mehdi Rezagholizadeh. Towards zero-shot knowledge distillation for natural language processing. In *Proceedings of the 2021 Conference on Empirical Methods in Natural Language Processing (EMNLP)*, pp. 6551–6561, 2021. doi: 10.18653/v1/2021.emnlp-main.526. URL https://aclanthology.org/2021.emnlp-main.526/.

Damien Robert, Hugo Raguet, and Loic Landrieu. Efficient 3d semantic segmentation with superpoint transformer. In *Proceedings of the IEEE/CVF International Conference on Computer Vision*, pp. 17195–17204, 2023.

Adriana Romero, Nicolas Ballas, Samira Ebrahimi Kahou, Antoine Chassang, Carlo Gatta, and Yoshua Bengio. Fitnets: Hints for thin deep nets. In Yoshua Bengio and Yann LeCun (eds.), *3rd International Conference on Learning Representations, ICLR 2015, San Diego, CA, USA, May 7-9, 2015, Conference Track Proceedings*, 2015. URL http://arxiv.org/abs/1412.6550.

Victor Sanh, Lysandre Debut, Julien Chaumond, and Thomas Wolf. Distilbert, a distilled version of BERT: Smaller, faster, cheaper and lighter. *arXiv preprint arXiv:1910.01108*, pp. 1–2, 2019.

Elchanan Solomon, Alexander Wagner, and Paul Bendich. From geometry to topology: Inverse theorems for distributed persistence. In *38th International Symposium on Computational Geometry (SoCG 2022)*, volume 224 of *Leibniz International Proceedings in Informatics (LIPIcs)*, pp. 61:1–61:16. Schloss Dagstuhl–Leibniz-Zentrum für Informatik, 2022. doi: 10.4230/LIPIcs.SoCG.2022.61.

Shuran Song, Fisher Yu, Andy Zeng, Angel X Chang, Manolis Savva, and Thomas Funkhouser. Semantic scene completion from a single depth image. In *Proceedings of the IEEE conference on computer vision and pattern recognition*, pp. 1746–1754, 2017.

Maomao Sun, Ting Rui, Jianqing Liu, Dong Wang, and Chengsong Yang. Enhancing lidar point cloud semantic segmentation via multiscale multiview fusion and knowledge distillation. *IEEE Sensors Journal*, Early Access, 2025.

Pei Sun, Henrik Kretzschmar, Xerxes Dotiwalla, Alexandre Chouard, Anand Patnaik, Paul Tsui, Yin Guo, Yuning Zhou, Yuning Chai, Benjamin Caine, et al. Scalability in perception for autonomous driving: Waymo open dataset. *Proceedings of the IEEE Conference on Computer Vision and Pattern Recognition (CVPR)*, pp. 2446–2454, 2020.

Tianfang Sun, Zhizhong Zhang, Xin Tan, Yong Peng, Yanyun Qu, and Yuan Xie. Uni-to-multi modal knowledge distillation for bidirectional lidar-camera semantic segmentation. *IEEE Transactions on Pattern Analysis and Machine Intelligence*, 46(12):11059–11072, 2024. doi: 10.1109/TPAMI.2024.3451658.

Haotian Tang, Zhijian Liu, Shengyu Zhao, Yujun Lin, Ji Lin, Hanrui Wang, and Song Han. Searching efficient 3d architectures with sparse point-voxel convolution. In *Computer Vision – ECCV 2020: 16th European Conference, Glasgow, UK, August 23–28, 2020, Proceedings, Part XXVIII*, volume 12373 of *Lecture Notes in Computer Science*, pp. 685–702. Springer, 2020.

Hugues Thomas, Charles R Qi, Jean-Emmanuel Deschaud, Beatriz Marcotegui, François Goulette, and Leonidas J Guibas. Kpconv: Flexible and deformable convolution for point clouds. In *Proceedings of the IEEE/CVF international conference on computer vision*, pp. 6411–6420, 2019.

Frederick Tung and Greg Mori. Similarity-preserving knowledge distillation. In *Proceedings of the IEEE/CVF international conference on computer vision*, pp. 1365–1374, 2019.

Peng-Shuai Wang, Yang Liu, Yu-Xiao Guo, Chun-Yu Sun, and Xin Tong. O-cnn: Octree-based convolutional neural networks for 3d shape analysis. *ACM Transactions On Graphics (TOG)*, 36(4):1–11, 2017.

Yue Wang, Yongbin Sun, Ziwei Liu, Sanjay E Sarma, Michael M Bronstein, and Justin M Solomon. Dynamic graph cnn for learning on point clouds. *ACM Transactions on Graphics (TOG)*, 38(5):1–13, 2019.

Zihan Wang, Yunhang Shen, Mengtian Li, Ke Li, Xing Sun, Shaohui Lin, and Lizhuang Ma. Knowledge transfer across modalities for weakly supervised point cloud semantic segmentation. In *2025 IEEE International Conference on Acoustics, Speech and Signal Processing (ICASSP)*. IEEE, 2025.

Xiaoyang Wu, Yixing Lao, Li Jiang, Xihui Liu, and Hengshuang Zhao. Point transformer v2: Grouped vector attention and partition-based pooling. In *Advances in Neural Information Processing Systems (NeurIPS)*, 2022a. URL `https://openreview.net/forum?id=I3mLa12s_H`.

Xiaoyang Wu, Yixing Lao, Li Jiang, Xihui Liu, and Hengshuang Zhao. Point transformer v2: Grouped vector attention and partition-based pooling. *Advances in Neural Information Processing Systems*, 35: 33330–33342, 2022b.

Xiaoyang Wu, Li Jiang, Peng-Shuai Wang, Zhijian Liu, Xihui Liu, Yu Qiao, Wanli Ouyang, Tong He, and Hengshuang Zhao. Point transformer v3: Simpler, faster, stronger. In *2024 IEEE/CVF Conference on Computer Vision and Pattern Recognition (CVPR)*, pp. 4840–4851, 2024. doi: 10.1109/CVPR52733.2024.00463.

Zhaoyang Xia, Youquan Liu, Xin Li, Xinge Zhu, Yuexin Ma, Yikang Li, Yuenan Hou, and Yu Qiao. SCPNet: Semantic scene completion on point cloud. In *Proceedings of the IEEE/CVF Conference on Computer Vision and Pattern Recognition (CVPR)*, pp. 17642–17651, 2023.

Jianyun Xu, Ruixiang Zhang, Jian Dou, Yushi Zhu, Jie Sun, and Shiliang Pu. Rpvnet: A deep and efficient range-point-voxel fusion network for lidar point cloud segmentation. In *Proceedings of the IEEE/CVF international conference on computer vision*, pp. 16024–16033, 2021.

Xu Yan, Jiantao Gao, Chaoda Zheng, Chao Zheng, Ruimao Zhang, Shuguang Cui, and Zhen Li. 2dpass: 2d priors assisted semantic segmentation on lidar point clouds. In *European Conference on Computer Vision*, pp. 677–695. Springer, 2022.

Yu-Qi Yang, Yu-Xiao Guo, Jian-Yu Xiong, Yang Liu, Hao Pan, Peng-Shuai Wang, Xin Tong, and Baining Guo. Swin3d: A pretrained transformer backbone for 3d indoor scene understanding. *arXiv preprint arXiv:2304.06906*, 2023.

Dongqiangzi Ye, Zixiang Zhou, Weijia Chen, Yufei Xie, Yu Wang, Panqu Wang, and Hassan Foroosh. Lidarmultinet: Towards a unified multi-task network for lidar perception. In *AAAI Conference on Artificial Intelligence*, 2022. URL `https://api.semanticscholar.org/CorpusID:252383236`.

Feihu Zhang, Jin Fang, Benjamin Wah, and Philip Torr. Deep fusionnet for point cloud semantic segmentation. In *Computer Vision–ECCV 2020: 16th European Conference, Glasgow, UK, August 23–28, 2020, Proceedings, Part XXIV 16*, pp. 644–663. Springer, 2020a.

Linfeng Zhang, Runpei Dong, Hung-Shuo Tai, and Kaisheng Ma. Pointdistiller: Structured knowledge distillation towards efficient and compact 3d detection. In *Proceedings of the IEEE/CVF Conference on Computer Vision and Pattern Recognition (CVPR)*, pp. 21791–21801, June 2023.

S. Zhang, J. Deng, L. Bai, et al. Hvdistill: Transferring knowledge from images to point clouds via unsupervised hybrid-view distillation. *International Journal of Computer Vision*, 132:2585–2599, 2024. doi: 10.1007/s11263-023-01981-w. URL `https://doi.org/10.1007/s11263-023-01981-w`.

Yang Zhang, Zixiang Zhou, Philip David, Xiangyu Yue, Zerong Xi, Boqing Gong, and Hassan Foroosh. Polarnet: An improved grid representation for online lidar point clouds semantic segmentation. In *Proceedings of the IEEE/CVF conference on computer vision and pattern recognition*, pp. 9601–9610, 2020b.

Hengshuang Zhao, Li Jiang, Chi-Wing Fu, and Jiaya Jia. Pointweb: Enhancing local neighborhood features for point cloud processing. In *Proceedings of the IEEE/CVF conference on computer vision and pattern recognition*, pp. 5565–5573, 2019.

Hengshuang Zhao, Li Jiang, Jiaya Jia, Philip H. S. Torr, and Vladlen Koltun. Point transformer. In *Proceedings of the IEEE/CVF International Conference on Computer Vision (ICCV)*, pp. 16259–16268, 2021. doi: 10.1109/ICCV48922.2021.01595. URL `https://openaccess.thecvf.com/content/ICCV2021/papers/Zhao_Point_Transformer_ICCV_2021_paper.pdf`.

Lin Zhao, Siyuan Xu, Liman Liu, Delie Ming, and Wenbing Tao. Svaseg: Sparse voxel-based attention for 3d lidar point cloud semantic segmentation. *Remote Sensing*, 14(18):4471, 2022.

Yin Zhou and Oncel Tuzel. Voxelnet: End-to-end learning for point cloud based 3d object detection. In *Proceedings of the IEEE Conference on Computer Vision and Pattern Recognition (CVPR)*, June 2018.

Xinge Zhu, Hui Zhou, Tai Wang, Fangzhou Hong, Yuexin Ma, Wei Li, Hongsheng Li, and Dahua Lin. Cylindrical and asymmetrical 3d convolution networks for lidar segmentation. In *Proceedings of the IEEE/CVF conference on computer vision and pattern recognition*, pp. 9939–9948, 2021.

Zhuangwei Zhuang, Rong Li, Kui Jia, Qicheng Wang, Yuanqing Li, and Mingkui Tan. Perception-aware multi-sensor fusion for 3d lidar semantic segmentation. In *Proceedings of the IEEE/CVF International Conference on Computer Vision (ICCV)*, pp. 16280–16290, 2021.

A Theoretical Foundations and Justifications

A.1 Topology of Feature vs. Topology of Spatial Coordinates

A critical distinction in our framework is the choice to distill the topology of latent feature spaces rather than physical spatial coordinates. This design is grounded in two fundamental geometric learning principles:

1. **Semantic vs. Physical Proximity:** Input spatial coordinates are constrained by Euclidean distance, capturing only physical proximity. In contrast, deep latent features evolve to capture semantic proximity. As demonstrated by Wang et al. (2019) in Dynamic Graph CNNs (DGCNN), feature-space neighborhoods in deeper layers group semantically similar objects (e.g., aggregating features from both the front and rear tires of a vehicle) even when they are geometrically distant. This allows the network to bypass physical distance, creating semantically coherent clusters that coordinate-based topology cannot capture.

2. **Invariance to Rigid Transformations:** Coordinate-based distillation objectives (e.g., Mean Squared Error on point coordinates) penalize any deviation in spatial alignment, making them sensitive to rotation and translation. Conversely, the topology of the feature space when characterized by persistent homology is theoretically invariant to such isometries. The Stability Theorem of persistence diagrams Cohen-Steiner et al. (2007) guarantees that topological descriptors depend solely on pairwise distances, rendering them invariant to the rigid transformation of the input. By aligning feature topology, we force the student to learn the intrinsic shape of the teacher's semantic manifold Moor et al. (2020), ensuring robust knowledge transfer that generalizes across geometric perturbations Jeon et al. (2024).

A.2 Subsampling and Stability of Vietoris–Rips Persistence

A major bottleneck in topological distillation is the computational cost of persistent homology (PH), which scales superlinearly with the number of points. We therefore compute PH on a subsample selected by Topology-Preserving Sampling (TPS) (Algorithm 5).

Let $H = \{h_1, \ldots, h_N\} \subset \mathbb{R}^C$ be the full feature set and let $H_I \subset H$ be the TPS subsample of size M. Define the (one-sided) covering radius

$$\varepsilon := \max_{x \in H} \min_{y \in H_I} \|x - y\|_2.$$

Because $H_I \subset H$, this equals the Hausdorff distance $d_H(H, H_I)$.

Proposition 1 (Rips interleaving under Hausdorff perturbations). Let A, B be finite subsets of a metric space $(\mathcal{X}, d)$ with $d_H(A, B) \leq \varepsilon$. Then the Vietoris–Rips filtrations $\mathrm{Rips}(A, r)$ and $\mathrm{Rips}(B, r)$ are 2ε-interleaved: for all $r \geq 0$,

$$\mathrm{Rips}(A, r) \to \mathrm{Rips}(B, r + 2\varepsilon) \quad \text{and} \quad \mathrm{Rips}(B, r) \to \mathrm{Rips}(A, r + 2\varepsilon),$$

via the nearest-neighbor correspondence. Consequently, their persistence modules are 2ε-interleaved, and the bottleneck distance between the corresponding persistence diagrams in any fixed homology dimension is at most 2ε.

Proof. For any edge (a, a') in $\mathrm{Rips}(A, r)$, choose $b, b' \in B$ with $d(a, b) \leq \varepsilon$ and $d(a', b') \leq \varepsilon$. By the triangle inequality, $d(b, b') \leq d(b, a) + d(a, a') + d(a', b') \leq r + 2\varepsilon$, so (b, b') is an edge in $\mathrm{Rips}(B, r + 2\varepsilon)$. This extends to all simplices, yielding a simplicial map. The reverse direction is analogous.

Implication for TPS. TPS directly minimizes the covering radius ε for a fixed budget M, so Proposition A.1 implies that the persistence diagrams computed on the TPS subset are a controlled approximation of the persistence diagrams of the full feature set, with error bounded (in bottleneck distance) by $O(\varepsilon)$. This motivates using TPS to reduce PH cost while preserving the dominant topological structures.

A.3 Noise Suppression via Persistence Weighting

This subsection provides the theoretical proof and Lemma 1 for Section 3.2.2, demonstrating how the logarithmic weighting function bounds the gradient influence of low-persistence features. It mathematically establishes that as the persistence of a topological feature approaches zero (representing noise), its contribution to the loss vanishes, thereby preventing the student model from overfitting to stochastic artifacts in the teacher's latent space.

Lemma 1 (Noise Suppression via Persistence Weighting)**.** *Let $\mathcal{D}^T$ and $\mathcal{D}^S$ be teacher and student persistence diagrams in a fixed homology dimension, containing only* finite *pairs. Define the persistence of a point $p = (b, d)$ as* $\mathrm{pers}(p) = d - b$*, and define the teacher weight*

$$w(p) = \log\big(1 + \mathrm{pers}(p)\big) \geq 0, \tag{9}$$

together with the stabilized normalizer

$$\bar{w}_T = \sum_{p \in \mathcal{D}^T} w(p) + \epsilon, \qquad \epsilon > 0. \tag{10}$$

Consider the weighted teacher-to-student Chamfer term

$$\mathcal{L}_{T \to S} = \frac{1}{\bar{w}_T} \sum_{p \in \mathcal{D}^T} w(p) \min_{q \in \mathcal{D}^S} \|p - q\|_2^2. \tag{11}$$

Then for any teacher point $p_0 \in \mathcal{D}^T$ with $\mathrm{pers}(p_0) = \delta$*, its contribution to $\mathcal{L}_{T \to S}$ is bounded by*

$$0 \leq \frac{w(p_0)}{\bar{w}_T} \min_{q \in \mathcal{D}^S} \|p_0 - q\|_2^2 \leq \frac{\log(1+\delta)}{\epsilon} \min_{q \in \mathcal{D}^S} \|p_0 - q\|_2^2. \tag{12}$$

In particular, as $\delta \to 0$ (near-diagonal/noisy features), $\log(1+\delta) \to 0$ *and this bound vanishes, so low-persistence teacher points have negligible influence on the weighted alignment term.*

Proof. The contribution of the Teacher's noise point p_{noise} to the Recall loss is given by:

$$L_p = d_{\min} \cdot \frac{w(p_{noise})}{\bar{w}_T} \tag{13}$$

Substituting the weight definition $w(p) = \log(1+\delta)$ and the normalization factor:

$$L_p = d_{\min} \cdot \frac{\log(1+\delta)}{\sum_k w(k) + \epsilon} \tag{14}$$

Using the first-order Taylor expansion $\log(1+x) \approx x$ for small δ, and observing that the denominator is strictly bounded below by ϵ (since $w(k) \geq 0$):

$$L_p \approx d_{\min} \cdot \frac{\delta}{\bar{w}_T} \leq d_{\min} \cdot \frac{\delta}{\epsilon} \tag{15}$$

Taking the limit as the persistence $\delta \to 0$:

$$\lim_{\delta \to 0} L_p \leq \lim_{\delta \to 0} \left(\frac{d_{\min}}{\epsilon} \cdot \delta \right) = 0 \tag{16}$$

Since $\bar{w}_T$ is bounded away from zero ($\bar{w}_T \geq \epsilon$), the denominator does not vanish. Consequently, as the persistence $\delta \to 0$, the loss contribution $L_p \to 0$ linearly. This ensures that the Student model is not penalized for ignoring negligible artifacts in the Teacher's latent space, allowing it to focus its representational capacity on matching persistent geometric structures.

□

B Efficient Implementation and Algorithms

B.1 Differentiable Feature-Space Distillation

This subsection details the complete forward and backward pass of the topological distillation framework (Algorithm 1). It outlines the specific sequence of operations—including feature normalization, Topology-Preserving Sampling (TPS), and the calculation of pairwise distances—required to route gradients through the critical edges of the Vietoris-Rips filtration.

Algorithm 1 Differentiable Feature-Space Topological Distillation (with Subgradient Routing)

Require: Student features $\mathbf{H}^S \in \mathbb{R}^{B\times N\times C_S}$, Teacher features $\mathbf{H}^T \in \mathbb{R}^{B\times N\times C_T}$
Require: Subsample size M (1024), stabilizer $\epsilon > 0$, tie tolerance τ_{tie}
Ensure: Topological Loss $\mathcal{L}_{topo}$
$\mathcal{L}_{topo} \leftarrow 0$
for $k = 1$ to B **do**
  // Step 1: Feature Normalization
  $\tilde{\mathbf{H}}^S \leftarrow \text{Normalize}(\mathbf{H}^S[k])$
  $\tilde{\mathbf{H}}^T \leftarrow \text{Normalize}(\mathbf{H}^T[k])$
  // Step 2: Topology-Preserving Selection (See Algorithm 5)
  $I_k \leftarrow \text{TPS}(\tilde{\mathbf{H}}^T, M)$
  $\mathbf{S} \leftarrow \tilde{\mathbf{H}}^S[I_k], \quad \mathbf{T} \leftarrow \tilde{\mathbf{H}}^T[I_k]$
  // Step 3: Distance Matrix Computation
  $\mathbf{D}^S \leftarrow \text{PairwiseDist}(\mathbf{S}), \quad \mathbf{D}^T \leftarrow \text{PairwiseDist}(\mathbf{T})$
  // Step 4: Topological Summarization (Forward with Tie-breaking)
  $\{\mathcal{D}_d^S\}_{d\in\{0,1\}} \leftarrow \text{DiffRipser}(\mathbf{D}^S; \tau_{\text{tie}})$
  $\{\mathcal{D}_d^T\}_{d\in\{0,1\}} \leftarrow \text{Ripser}(\mathbf{D}^T)$
  // Step 5: Persistence Weighted Chamfer Distance (See Algorithm 2)
  for $d \in \{0, 1\}$ **do**
    $\mathcal{L}_{topo} \leftarrow \mathcal{L}_{topo} + \text{PWCD}(\mathcal{D}_d^T, \mathcal{D}_d^S; \epsilon)$
  end for
end for
return $\mathcal{L}_{topo}/B$

B.2 Persistence-Weighted Chamfer Loss

This subsection defines the specialized loss function used to align the persistence diagrams of the student and teacher. It explains the logarithmic weighting mechanism designed to suppress low-persistence sampling noise while prioritizing robust topological features like loops and clusters during optimization (Algorithm 2).

B.3 Implementation of Gradient Routing

While persistent homology is computed by discrete operations (sorting simplices and boundary-matrix reduction), the birth/death times are piecewise-smooth functions of the underlying pairwise distances. For the Vietoris–Rips filtration (simplex filtration value equals the maximum edge length), each birth/death value is realized by one or more maximizer edges in the distance matrix. At degenerate configurations where multiple edges tie for the same filtration value, the gradient is not unique; we use a standard subgradient convention by averaging the gradient uniformly over all tied maximizer edges. This yields stable optimization and avoids relying on fragile uniqueness assumptions. The method is described in Algorithm 3.

B.4 Complexity Reduction via Topology-Preserving Selection

To implement efficient subsampling, we employ Topology-Preserving Sampling (TPS), which is a greedy approximation to the k-center problem. TPS explicitly minimizes the covering radius (and thus the Hausdorff

Algorithm 2 Persistence-Weighted Chamfer Loss

Require: Teacher diagram $\mathcal{P}^T = \{p_i\}_{i=1}^M \subset \mathbb{R}^2$; Student diagram $\mathcal{P}^S = \{q_j\}_{j=1}^N \subset \mathbb{R}^2$; stabilizer $\epsilon > 0$.
Ensure: Topology loss $\mathcal{L}_{\text{topo}}$.

// 1) Trivial case
if $M = 0 \wedge N = 0$ **then**
  return 0
end if
// 2) Teacher weights
if $M > 0$ **then**
  $WT[i] \leftarrow log(1 + max(p_i^{(2)} - p_i^{(1)}, 0))$ # $p = (b, d)$
  $\bar{W}_T \leftarrow \sum_{i=1}^M W_T[i] + \epsilon$
end if
// 3) Helper: squared distance to diagonal
$\text{dist}_\Delta^2(b, d) \leftarrow \frac{(d-b)^2}{2}$
// 4) If both non-empty, compute pairwise costs
if $M > 0 \wedge N > 0$ **then**
  $C_{ij} \leftarrow \frac{1}{2}\|p_i - q_j\|_2^2$ # $M \times N$
end if
// 5) Recall term (Teacher → Student) with diagonal fallback
if $M = 0$ **then**
  $L_{\text{recall}} \leftarrow 0$
else if $N = 0$ **then**
  $L_{\text{recall}} \leftarrow \frac{1}{\bar{W}_T} \sum_{i=1}^M W_T[i] \, \text{dist}_\Delta^2(p_i^{(1)}, p_i^{(2)})$
else
  $\min_{T \to S}[i] \leftarrow \min_j C_{ij}$
  $L_{\text{recall}} \leftarrow \frac{1}{\bar{W}_T} \sum_{i=1}^M W_T[i] \; \min\Big\{\min_{T \to S}[i], \text{dist}_\Delta^2(p_i^{(1)}, p_i^{(2)})\Big\}$
end if
// 6) Precision term (Student → Teacher) with diagonal fallback
if $N = 0$ **then**
  $L_{\text{prec}} \leftarrow 0$
else if $M = 0$ **then**
  $L_{\text{prec}} \leftarrow \frac{1}{N} \sum_{j=1}^N \text{dist}_\Delta^2(q_j^{(1)}, q_j^{(2)})$
else
  $\min_{S \to T}[j] \leftarrow \min_i C_{ij}$
  $L_{\text{prec}} \leftarrow \frac{1}{N} \sum_{j=1}^N \min\Big\{\min_{S \to T}[j], \text{dist}_\Delta^2(q_j^{(1)}, q_j^{(2)})\Big\}$
end if
return $L_{\text{recall}} + L_{\text{prec}}$

distance) between the selected subset and the full feature set. This directly reduces the worst-case approximation error of geometric/topological summaries under a fixed budget. We use TPS to select indices, then compute PH only on the selected subset. The algorithm is described in Algorithm 5.

Quantitative Efficiency Analysis. To validate the computational efficiency of our hybrid pipeline (combining the Ripser Bauer (2021), critical-edge gradient routing, and TPS), we benchmark the total forward-and-backward runtime against a naive pure-PyTorch implementation. As shown in Table 8, the naive approach suffers from combinatorial complexity explosion, becoming computationally intractable beyond $N = 100$ and exhausting GPU memory at $N = 200$. In contrast, our method maintains real-time performance, achieving speedup factors exceeding $10,000\times$ at $N = 100$ and scaling efficiently to $N = 1024$ with negligible overhead.

Algorithm 3 Critical-Edge Gradient Routing

Require: Student features $F \in \mathbb{R}^{N\times C}$; teacher diagrams $\{P_T^{(d)}\}_{d\in\{0,1\}}$; stabilizers $\varepsilon_{\text{dist}}, \varepsilon_w > 0$; tie tolerance τ_{tie}.
Ensure: Feature gradients $\nabla_F \mathcal{L}$.

Compute distance matrix D: $D_{ij} \leftarrow \|F_i - F_j\|_2$ for $1 \le i < j \le N$.
Initialize edge accumulator $G \in \mathbb{R}^{N\times N}$ with zeros.
for $d \in \{0, 1\}$ **do**
  // Forward pass: compute diagrams and extract critical simplices
  Run Ripser(D) to obtain student diagram $P_S^{(d)}$ and pairing map $\Pi^{(d)}$.
  Compute diagram gradients: $(g_b, g_d) \leftarrow \text{PWCDGrad}(D_T^{(d)}, D_S^{(d)}; \varepsilon_w)$ *// See algorithm 4.*
  for $k = 1$ **to** $|D_S^{(d)}|$ **do**
    Let $(\sigma_{\text{birth}}, \sigma_{\text{death}}) \leftarrow \Pi^{(d)}(k)$.
    // Route birth gradient (only for H_1)
    if $d = 1$ **then**
      Let $\{i, j\} = \sigma_{\text{birth}}$.
      $G_{ij} \leftarrow G_{ij} + g_b[k]$.
    end if
    // Route death gradient
    if $d = 0$ **then**
      Let $\{u, v\} = \sigma_{\text{death}}$ be the destroying edge.
      $G_{uv} \leftarrow G_{uv} + g_d[k]$.
    else
      // For H_1, death is caused by a triangle $\{a, b, c\}$ completing a cycle
      Let $E_\Delta = \{(a, b), (b, c), (a, c)\}$.
      $m \leftarrow \max_{(u,v)\in E_\Delta} D_{uv}$.
      $E^\star \leftarrow \{(u, v) \in E_\Delta : |D_{uv} - m| \le \tau_{\text{tie}}\}$.
      for each $(u, v) \in E^\star$ **do**
        $G_{uv} \leftarrow G_{uv} + g_d[k]/|E^\star|$.
      end for
    end if
  end for
end for
// Backpropagate distances to features
Initialize $\nabla_F \mathcal{L} \leftarrow \mathbf{0}$.
for $1 \le i < j \le N$ **do**
  if $G_{ij} \neq 0$ **then**
    $u_{ij} \leftarrow (F_i - F_j)/(D_{ij} + \varepsilon_{\text{dist}})$.
    $\nabla_{F_i} \mathcal{L} \leftarrow \nabla_{F_i} \mathcal{L} + G_{ij} \cdot u_{ij}$.
    $\nabla_{F_j} \mathcal{L} \leftarrow \nabla_{F_j} \mathcal{L} - G_{ij} \cdot u_{ij}$.
  end if
end for
return $\nabla_F \mathcal{L}$.

C Experimental Setup and Hyperparameters

C.1 Datasets

SemanticKITTI Behley et al. (2019) provides LiDAR point clouds from urban and suburban scenes, featuring 22 sequences with dense semantic annotations across 19 classes (e.g., vehicles, pedestrians, roads). Its high resolution and detailed labels make it a rigorous testbed for semantic segmentation.

NuScenes Caesar et al. (2020) integrates LiDAR, camera, and radar data in 1,000 diverse scenes, including urban roads and highways. With 3D bounding box annotations for 23 object types, it challenges models with varied weather, occlusions, and dynamic elements suited for detection and segmentation tasks. In addition, we use nuScenes-lidar seg, which is an extension of nuScenes. This dataset has semantic labels of 32 categories and annotates each point from keyframes in nuScenes. We used the 700 scenes in the training

Algorithm 4 PWCDGrad: Diagram-space gradients for Persistence-Weighted Chamfer Distance

Function PWCDGrad(D_T, D_S, ε_w):
  Input: Teacher $D_T = \{p_i\}_{i=1}^{M}$, Student $D_S = \{q_k\}_{k=1}^{K}$, stabilizer ε_w
  Output: Gradient arrays g_b, g_d of size K
  Initialize $g_b \leftarrow \mathbf{0},\ g_d \leftarrow \mathbf{0}$
  Define $w(b, d) = \log(1 + \max(d - b, 0))$
  Compute $\bar{w}_T = \varepsilon_w + \sum_{i=1}^{M} w(b_i^T, d_i^T)$
  // 1. Recall Term (Teacher → Student)
  if $M > 0$ **and** $K > 0$ **then**
    for $i = 1$ **to** M **do**
      $k^\star \leftarrow \arg\min_k \|q_k - p_i\|_2^2$ *// Find nearest student*
      $dist_{match} \leftarrow \|q_{k^\star} - p_i\|_2^2$
      $dist_{diag} \leftarrow \frac{1}{2}(d_i^T - b_i^T)^2$
      if $dist_{match} \le dist_{diag}$ **then**
        $s \leftarrow w(b_i^T, d_i^T)/\bar{w}_T$
        $g_b[k^\star]$ += $2s \cdot (b_{k^\star} - b_i^T)$
        $g_d[k^\star]$ += $2s \cdot (d_{k^\star} - d_i^T)$
      end if
    end for
  end if
  // 2. Precision Term (Student → Teacher)
  if $K > 0$ **then**
    for $k = 1$ **to** K **do**
      $q_k \leftarrow (b_k, d_k)$
      $is\_matched \leftarrow$ **false**
      if $M > 0$ **then**
        $i^\star \leftarrow \arg\min_i \|q_k - p_i\|_2^2$ *// Find nearest teacher*
        $dist_{match} \leftarrow \|q_k - p_{i^\star}\|_2^2$
        $dist_{diag} \leftarrow \frac{1}{2}(d_k - b_k)^2$
        if $dist_{match} \le dist_{diag}$ **then**
          $g_b[k]$ += $\frac{2}{K}(b_k - b_{i^\star}^T)$
          $g_d[k]$ += $\frac{2}{K}(d_k - d_{i^\star}^T)$
          $is\_matched \leftarrow$ **true**
        end if
      end if
      // Fallback to diagonal if no match found or teacher empty
      if not $is\_matched$ **then**
        $\delta \leftarrow d_k - b_k$
        $g_b[k]$ −= $\frac{1}{K}\delta$
        $g_d[k]$ += $\frac{1}{K}\delta$
      end if
    end for
  end if
  return (g_b, g_d)

set with segmentation labels to fine-tune for the semantic segmentation task, and the 150 scenes in the validation set to verify the performance.

Waymo Open Dataset Sun et al. (2020) delivers high-resolution LiDAR data from 1,000 segments in various locations, with frequent sweeps and 3D annotations for vehicles, pedestrians and cyclists. Its long-range scans and varied conditions test robustness and generalization.

C.2 Model Configuration and Training

We use Point Transformer V3 Wu et al. (2024) as the backbone. The student model is approximately 20% the depth of the teacher, trained from scratch.

Algorithm 5 Topology-Preserving Sampling (TPS)

Require: Feature set $\mathcal{H} = \{h_1, \ldots, h_N\}$, target size M
Ensure: Indices $I \subset \{1, \ldots, N\}$ with $|I| = M$
Initialize $I \leftarrow \{i_1\}$ (random index); $D_{\min}[i] \leftarrow \|h_i - h_{i_1}\|_2$
for $k = 2$ to M **do**
  $i_k \leftarrow \arg\max_i D_{\min}[i]$
  $I \leftarrow I \cup \{i_k\}$
  $D_{\min}[i] \leftarrow \min\big(D_{\min}[i], \|h_i - h_{i_k}\|_2\big) \quad \forall i$
end for
return I

	Naive Baseline			Ours			
Input (N)	**Fwd (s)**	**Bwd (s)**	**Mem (MB)**	**Fwd (s)**	**Bwd (s)**	**Mem (MB)**	**Speedup**
30	19.31	0.12	17.1	0.24	0.002368	8.2	79×
60	321.12	0.32	40.2	0.05	0.000250	16.5	6,039×
100	963.30	1.06	128.6	0.14	0.000254	17.3	6,743×
200	*Infeasible (Timeout)*			0.36	0.000271	22.7	—
400	*Infeasible (Timeout)*			0.30	0.000265	29.1	—
800	*Infeasible (Timeout)*			0.40	0.000236	42.0	—
1024	*Infeasible (Timeout)*			0.37	0.000258	49.1	—

Table 8: **Computational Efficiency Benchmark.** Comparison of Forward (Fwd) and Backward (Bwd) pass runtimes and Peak Memory usage. While the Naive implementation suffers from cubic complexity, becoming infeasible beyond $N = 100$, our method maintains sub-second latency even at $N = 1024$.

- **Encoder Depths:** Teacher $(2, 2, 2, 6, 2)$ → Student $(1, 1, 1, 2, 1)$.
- **Encoder Channels:** Teacher $(32, 64, 128, 256, 512)$ → Student $(16, 16, 32, 64, 128)$.
- **Attention Heads:** Scaled down from Teacher $(2, 4, 8, 16, 32)$ to Student $(1, 1, 2, 4, 8)$.

Training Protocol. Models are trained for 50 epochs (batch size 12) using AdamW (LR 0.002, Weight Decay 0.005) with a OneCycleLR scheduler to ensure stable convergence and effective generalization. We employ a two-stage distillation strategy: the teacher is pre-trained to convergence before guiding the student.

C.3 Data Augmentation and Resources

We apply random rotation ($\pm 1°$), uniform scaling ($0.9 - 1.1\times$), random flipping, and Gaussian jittering ($\sigma = 0.005$) before grid sampling (0.05 m). All experiments were conducted on a University HPC Cluster node equipped with 2 NVIDIA A100 GPUs (81 GB VRAM).

D Additional Ablation and Sensitivity Analysis

D.1 Visualization

To intuitively assess the effectiveness of our distillation framework, we visualize the semantic segmentation predictions on the nuScenes validation set in Figure 3. The comparison includes the Ground Truth (a), the Teacher's prediction (b), and the Student's prediction (c). As observed, the Teacher model (b) generates high-fidelity predictions that closely align with the Ground Truth (a), particularly in capturing complex structural layouts such as road boundaries and vehicle clusters. Crucially, the Student model (c), despite its reduced capacity, successfully replicates this performance. The Student accurately preserves the global topology of the scene. Large-scale connected components, such as the drivable surface (brown) and the surrounding road network, are segmented with high continuity, which is effectively minimizing fragmentation. This contributes

to our Topological Distillation, which enforces the preservation of persistent geometric features like loops and clusters Hu et al. (2019). Additionally, small and scattered classes, such as vegetation (green points) and thin linear structures like barriers (gray lines), are sharply resolved. Standard distillation methods often fail to capture these high-frequency details due to limited receptive fields or effective context aggregation Liu et al. (2019a). The sharpness of these boundaries in Figure 3c confirm that our Saliency-Aware Alignment successfully focused the Student's attention on these spatially discriminative regions, preventing them from being washed out by the dominant background classes.

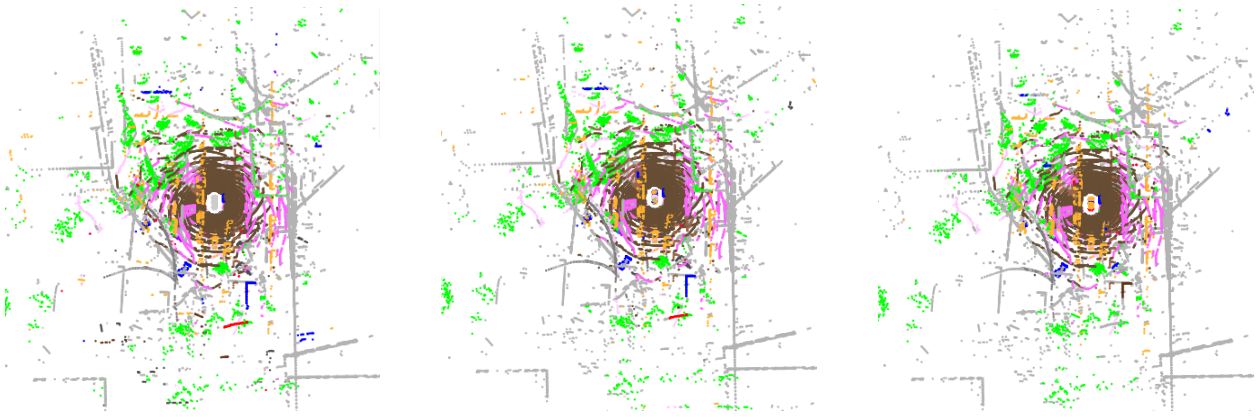

(a) Ground Truth (b) Teacher Prediction (c) Student Prediction

Figure 3: Visualization of our method on the nuScenes validation set. (a) Ground truth, (b) teacher model prediction, and (c) student model prediction. The student model closely follows the teacher's output and ground truth, successfully capturing almost all object classes, demonstrating the effectiveness of the knowledge distillation process.

Figure 4 illustrates how persistent homology captures the evolution of topological features across different filtration scales. Given a point cloud, we construct a simplicial complex and track the birth and death of topological structures as the filtration parameter ϵ increases. The persistence diagram $D = \{(b_i, d_i)\}_{i=1}^{M}$ quantifies these events, where each point represents a topological feature. Longer bars correspond to persistent structures that encode essential geometric patterns, while shorter bars typically represent noise or minor perturbations.

Visualizing the persistence diagrams allows us to better understand the types of geometric features captured by the teacher model, such as connected components (H_0), loops (H_1) and voids (H_2). By encouraging the student to mimic these persistent topological features through topology-aware distillation, we aim to transfer not only semantic knowledge but also the critical underlying geometric structures necessary for robust point-cloud understanding. This visualization supports the intuition behind our method, showing that topological summaries can effectively reflect meaningful geometric information beyond what is captured by the Euclidean feature alignment.

D.2 Topological Sensitivity

Homology Dimension (H_1 vs. H_2). We restrict our experiments to H_0 and H_1. As shown in Figure 6, extending to H_2 causes factorial runtime growth due to the combinatorial explosion of 2-simplices (triangles) required for the filtration. Specifically, while the number of edges scales quadratically, the number of triangles scales cubically, causing the boundary matrix reduction step to become a computational bottleneck. Our benchmark reveals that for inputs as small as $N = 400$, computing H_2 incurs a latency spike orders of magnitude higher than H_1, making it infeasible for iterative training. Furthermore, for surface-based 2.5D LiDAR data, H_2 (voids) offers diminishing returns compared to clustering (H_0) and loops (H_1). Since LiDAR scans capture the *boundary* of objects rather than their volume, genuine enclosed voids are rarely observed; the topological signal is predominantly carried by 1-dimensional cycles (e.g., window frames, poles, and tires), which are fully captured by H_1.

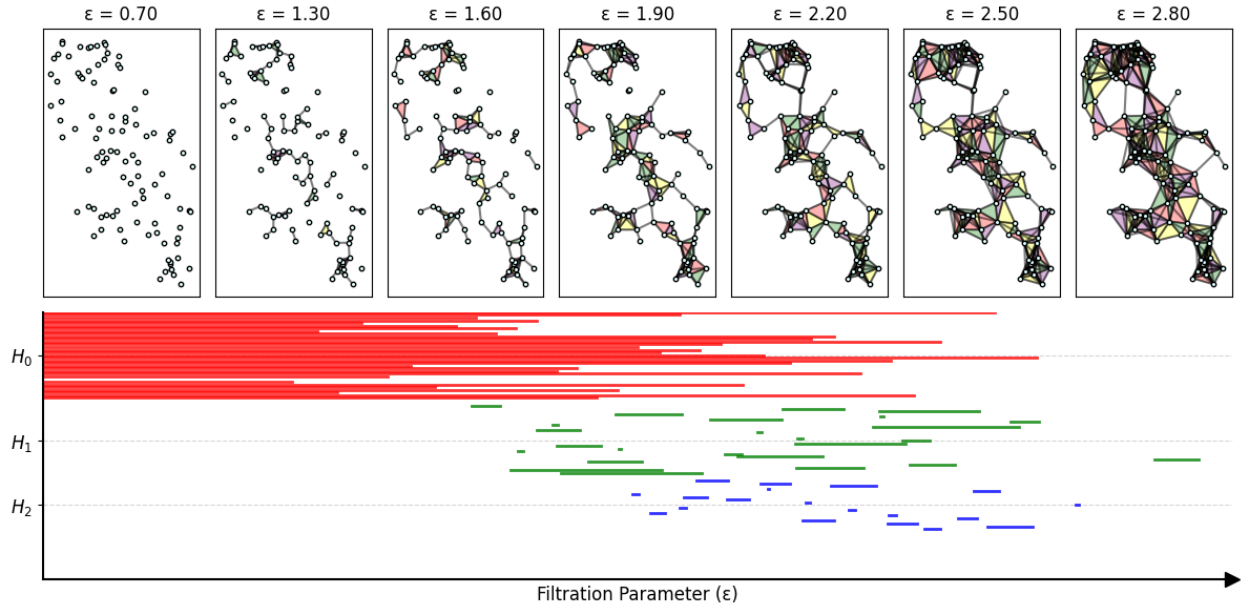

Figure 4: Visualization of topology-aware analysis through Vietoris–Rips filtration. The top row depicts the evolution of the simplicial complex as the filtration parameter ϵ increases. The bottom part shows the corresponding barcode representation of persistent homology groups in different dimensions (H_0, H_1, H_2).

Noise Mitigation. Standard topological loss functions are often hypersensitive to sampling noise, treating transient, short-lived features with the same importance as robust structural loops. To prevent the student from overfitting to these artifacts, we introduce a logarithmic weighting function, $w(p) = \log(1 + \text{pers}(p))$, which scales the gradient magnitude based on feature persistence. As demonstrated in Figure 7, this function effectively suppresses the gradients for low-persistence noise ($p \approx 0$) while preserving strong training signals for high-persistence structural features. This ensures the student minimizes the impact of sampling anomalies and focuses solely on learning the robust manifold topology.

D.3 Validation of Topological Correctness

To ensure the validity of our custom PyTorch implementation, we verified that it produces persistence diagrams topologically equivalent to the C++ `Ripser` library Bauer (2021). Figure 8 demonstrates this alignment across different geometric primitives.

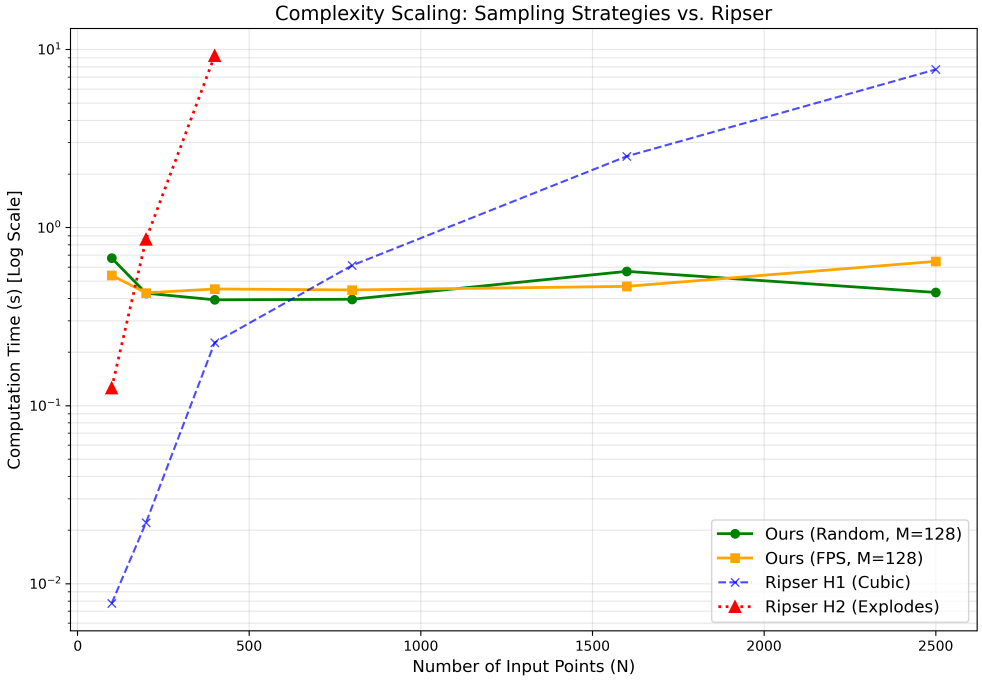

Figure 5: **Complexity Scaling of Subsampling Strategies.** Comparison of computation time between Topology-Preserving Sampling (TPS) as a function of input point cloud size N, with a fixed subsample size $M = 128$. Random sampling maintains nearly constant time, whereas TPS scales linearly with N, highlighting the trade-off between geometric coverage and computational efficiency for large inputs.

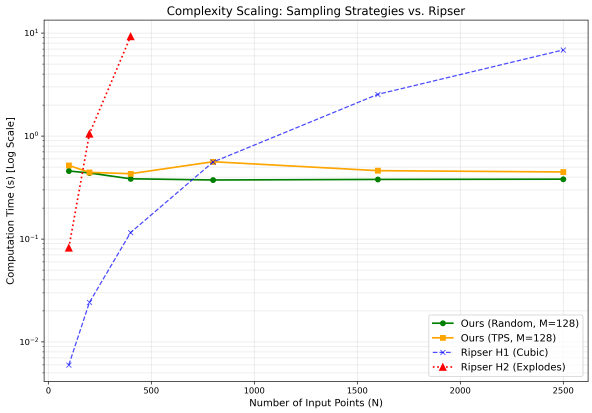

Figure 6: **Complexity Scaling (H_1 vs. H_2).** H_2 computation is intractable for training loops.

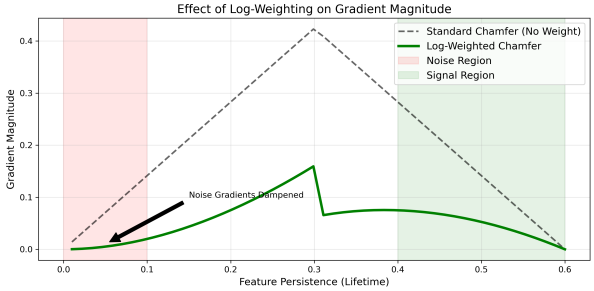

Figure 7: **Gradient Dampening.** Log-weighting suppresses noise (red) vs signal (green).

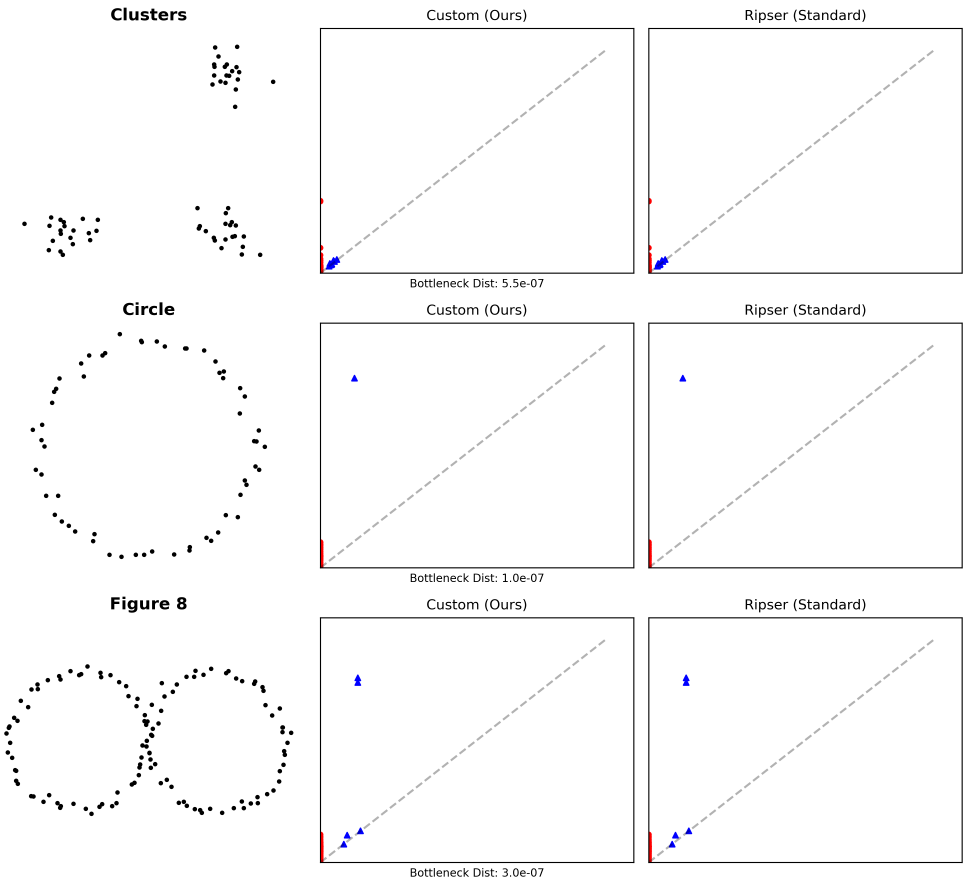

Figure 8: **Validation of Topological Correctness.** Visual comparison of persistence diagrams generated by our pure-PyTorch baseline versus `Ripser`. The diagrams are topologically equivalent with negligible bottleneck distances.